Kilometer-scale Transient Atmospheres for Kinetic Payload Deposition on Icy Bodies

James Koch

A thesis

submitted in partial fulfillment of the

requirements for the degree of

Master of Science in Aeronautics and Astronautics

University of Washington

2017

Committee:

Robert Winglee, Chair

Carl Knowlen

Program authorized to offer degree:

Aeronautics and Astronautics

University of Washington

Abstract

Kilometer-scale Transient Atmospheres for Kinetic Payload Deposition on Icy Bodies

James Koch

Chair of the Supervisory Committee:

Dr. Robert Winglee, Professor

Earth and Space Sciences

Entry, descent, and landing technologies for space exploration missions to atmospheric bodies traditionally exploit the body's ambient atmosphere as a medium through which a spacecraft or probe can interact to transfer momentum and energy for a soft landing. For bodies with no appreciable atmosphere, a significant engineering challenge exists to overcome the lack of passive methods to decelerate a spacecraft or probe. Proposed is a novel means for the creation of a transient atmosphere for airless icy bodies through the use of a two stage payload-penetrator probe. The first stage is a hyper-velocity penetrator that impacts the icy body. The second stage is an aero-braking-capable probe directed to pass through the ejecta plume from the hyper-velocity impact. Both experimental and computational studies show that a controlled high-energy impact can direct and transfer energy and momentum to a probe via a collimated ejecta plume. In an effort to provide clarity to this unexplored class of missions, a modeling-based engineering approach is

taken to provide a first-order estimation of some of the involved physical phenomena.

Three sub-studies are presented: an examination and characterization of ice plumes, modeling plume-probe interaction, and the extension of plume modeling as the basis for conceptual mission design. The modeling efforts are centered about two modeling formulations: smoothed particle hydrodynamics (SPH) and the arbitrary Largrangian-Eulerian (ALE) set of techniques. A database of fully-developed hypervelocity impacts and their associated plumes is created and used as inputs to a 1-D mathematical model for the interaction of a continuum-based plume and probe. A parametric study based on the hyper-velocity impact and staging of the probe-penetrator system is presented and discussed. Shown is that a tuned penetrator-probe mission has the potential to increase spacecraft payload mass fraction over conventional soft landing schemes.

Contents

List of Figures

List of Tables

Chapter 1

Europa, Extra-Terrestrial Life, and Space Exploration

Perhaps the biggest driver in modern space exploration is the prospect of finding life (or life-like signatures) in neighboring celestial bodies. Several of the science objectives of the Mars rovers (including those of the Mars 2020 program) were to probe the Martian environment to give more insight into what the composition of the planet is and how it compares to that of the Earth. Questions that are actively being investigated include: what organic compounds exist on the planet? How does the through-thickness of the Martian soil vary? What is the composition of the atmosphere? Is water present in any of these domains? On Earth, wherever scientists have found bodies of water, life in some form has also been found, even in extreme environments such as high pressure and temperature areas around deep sea vents or in super-cooled water pockets well beneath surface ice in areas close to the poles. The question is then whether these observations are extensible to other planetary bodies.

Mars is not the only candidate for life besides Earth in our solar system. Europa, the sixth moon of Jupiter and the focus of this study, is believed to hold a vast under-ice liquid water ocean (Figure 1.1). This ocean is kept in its liquid state through the severe

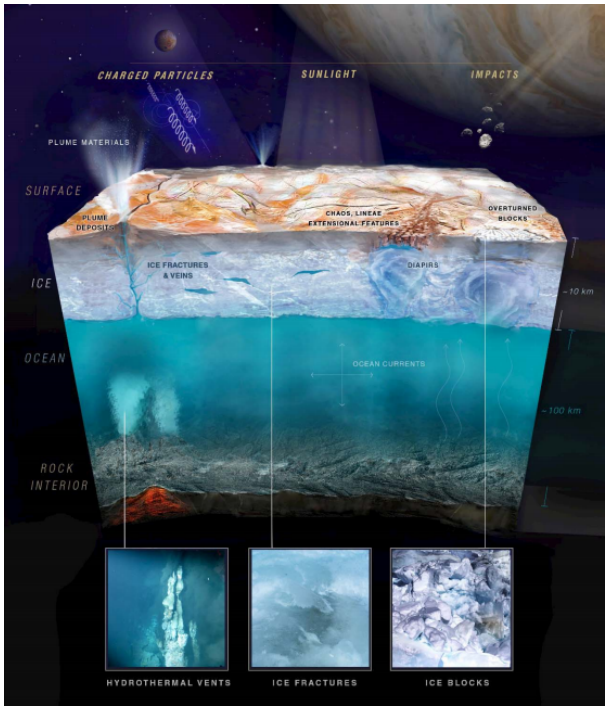

Figure 1.1: A through-thickness overview of Europa. Courtesy of NASA/JPL-Caltech.

tidal flexing from its gravitational interaction with Jupiter and its other moons. As such, this ocean world has captivated the minds of scientists and engineers for years. Adding to the mysticism of this moon is the potential to actually probe the moon with a NASA mission to this moon.

1.1 Entry, Decent, and Landing Systems

The engineering problem of extra-terrestrial exploration is driven by the need for simple, robust, and (relatively) low-cost methods to observe objects of interest. Though no mission to directly observe an extra-terrestrial body is simple, the design philosophy and physics behind the missions should yield to well-understood and repeatable concepts while satisfying mission requirements. Likewise, the technology behind these missions should be robust in the sense that the technology can deliver the performance required by the mission with complete certainty. Lastly, missions cannot be prohibitive in cost,

lest the mission become a purely academic design study. This cost constraint is closely related to weight and payload fraction - two critical parameters for space missions.

Technological innovation is derived from engineering and scientific constraints. These constraints may remain largely the same (in language) for most exploration and scientific missions. However, for future exotic missions, implied is that the current 'status quo' of sending large, heavy, and expensive landers and probes may not fly, especially for such high-profile missions involving "unconventional" destinations like moons or asteroids.

The Sky Crane was developed to meet the unique challenges associated with a mission to Mars [6]. Mars has an atmosphere roughly 100 times thinner than that of Earth [7]. For payloads of appreciable mass, such as the Mars rovers, this provides a challenge for landing the payload on the surface of Mars without damage to the payload and ensuring landing success. The Sky Crane was developed in response to the entry, decent, and landing requirements of the mission payload, since aero-braking (drag) alone cannot dissipate enough kinetic energy (either through heat or momentum transfer) to land the rovers on the surface of Mars. The Sky Crane employs retro-grade rocket thrusters to decelerate and vector the rover decent assembly safely to the surface [8]. NASA'a official concept image for the system is pictured in Figure 1.2. Of note is the fact that a parachute was still deployed in the hypersonic regime where drag is appreciable, adding another layer of systems integration and complexity. Given the success of the deceleration system on Mars, this system is currently the leading option for the Europa Lander mission planned for the mid 2020's [9].

The systems developed specifically because Mars, Europa, and other celestial bodies do not have appreciable atmospheres are complex, expensive, and heavy. This is the motivation for creating a transient atmosphere around a potential landing area. Should such an atmosphere exist, no matter how thin, the potential for passive energy dissipation increases. In the limit, one can use Earth's atmosphere as an example case for passive entry, meaning that no energy must be expelled by the system to decelerate. The Space Shuttles are excellent examples of this. Upon hypersonic entry, the shuttles

Figure 1.2: An artist's rendition of the Mars Science Laboratory Sky Crane landing system. Courtesy NASA/JPL-Caltech.

dissipate much of their kinetic energy through drag and are able to glide through the full atmospheric profile to a runway for horizontal landing.

Perhaps it is possible to restructure an exploration mission (such as the proposed Europa lander mission) to passively dissipate the great deal of stored kinetic energy in the craft's motion through more efficient momentum transfer. Likewise, the total mass and volume constraints on such a mission could also be reduced, since the need for complex decent systems would no longer be necessary, thus potentially increasing mission scope and payload mass fraction. This study sets up the tools to design kinetic penetrators for passive entry, decent, and landing on airless bodies and presents preliminary results to show the effectiveness of these tools.

1.2 Planetary Penetrators

Several forms of planetary penetrators have been used or proposed in recent history. Perhaps most notable are the military applications of ground-penetrating ordinances reliant on penetration depth through dense and hard materials for effective deployment. Regolith penetrators have also been proposed for payload deposition (or sub-surface

observation) of foreign worlds and for sample return missions for extreme environments.

1.2.1 Munitions

'Bunker busters' (also called Earth-Penetrating Weapons or Massive Ordinance Penetrator), are a type of munition designed specifically to deliver an explosive payload deep beneath the Earth's surface where a fortified bunker or storage complex may be. Bunker busters are not a new technology. They date back to World War II when both the Royal Air Force and the German forces independently developed bombs capable of penetrating reinforced concrete [10]. These munitions relied on the penetration depth of the articles to reach the levels of the foundations of the enemy structures such that the structures would collapse into the void left by the ordinance blast. During this arms race between sides, the concept of sectional density (a measure of the distribution of an ordinance's mass to its cross-sectional area) was proposed by August Cönders [10]. This provided a design parameter that could readily be correlated to penetration depth. More recent advancements in penetrating ordinances include the use of hard, exotic materials to promote deeper penetration as well as variable-sectional density designs for tunable performance [11]. An example of a tuned system is the General Dynamics BLU-122 ground penetrator, shown in action in Figure 1.3. Of note is the shape (an ogive curve) and preservation of the penetrator tip and the ejecta pattern - there is a significant mass flux away from the impact plane in the direction opposite that of the penetrator. Bunker busters have proven been very successful in the field, with some munitions (like the BLU-122) penetrating over 100 feet through reinforced concrete from a passive aircraft delivery [11].

1.2.2 Payload Deposition

Kinetic penetrators have been proposed for planetary science missions. To gain knowledge of the Martian regolith, the proposed NASA-Hughes Mars Pioneer Mission (1974) featured

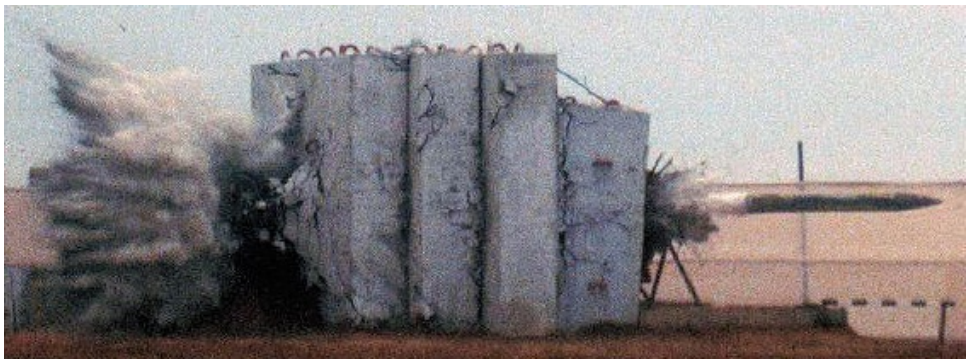

Figure 1.3: General Dynamics BLU-122 Penetrator with 'enhanced blast and fragmentation'. Image credit: General Dynamics

prominently a set of kinetic penetrators for the deposition of scientific instruments into the Martian surface[1]. This planned mission was full of unconventional techniques for achieving the science mission. First, the orbiter itself had no scientific payload. The payloads were contained within six penetrators housed on board the orbiter. These were launched with conventional TOW missile launchers. The NASA technical document for the mission claims that an elliptical area of 100km by 10km could be hit (3σ), which was an incredible degree of confidence in the deployment and systems engineering of the mission. The penetrators housed deboost motors for rapid deceleration as well as relying on the thin Martian atmosphere for stability and some degree of drag. While this mission did not come to fruition, the engineering exercise of planning a six-penetrator mission architecture revealed significant advantages to a penetrator-based mission over a conventional orbiter with on-board science payloads. Most significantly, the mission itself was more mass efficient than the non-penetrator based Pioneer missions of the same class (more science per mass). In addition, the proposed science was through direct contact, not remote sensing. The proposed scientific payload contained within a mock penetrator is shown in Figure 1.4.

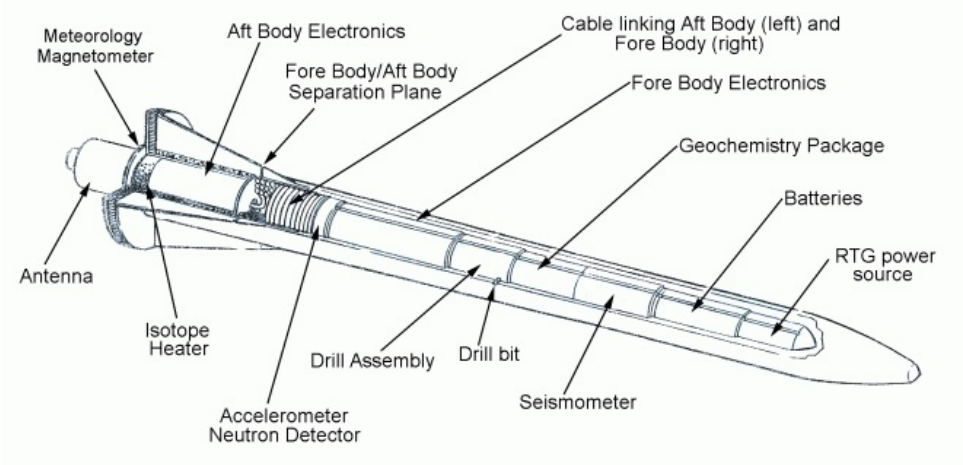

Figure 1.4: Hughes' proposed penetrator architecture for a Martian Pioneer Mission [1].

1.2.3 Sample Return Missions

Truitt [12] has demonstrated the effectiveness of high-velocity penetrators in rock coring as a means for sample retrieval for sample return missions in extreme environments. In this study, penetrators field tested at 300-600 m/s were used successfully for rock coring and sample ejection. Again, the mass flux in the direction opposite of that of the penetrator is quite significant, with sample yield on the order of kilograms (3.2kg for a sandstone impact) ejected at a few percent of the impact velocity. The experimental results are unique because of the use of the spalling and ejection processes during cratering to create and separate the rock cores from the rest of the surrounding material.

1.2.4 Extension to Staged Impacts and Ejecta Braking

Recent studies at the University of Washington Advanced Propulsion Laboratory have sought to exploit the mass flux rearwards from the ejection processes of high velocity impacts into ice for the development of drag on subsequent stages [13]. Included in these studies were the comparison of the cratering and ejection processes for conical projectiles and cylindrical projectiles. In the impacts for sharp cones, typical (meaning reasonable agreement with published empirical penetration depth and cratering relations)

cratering and ejection behavior was observed. For hollow cylindrical projectiles, high velocity impacts yielded collimated plumes of ice. Preliminary simulations of cylindrical steel penetrators into concrete (concrete has similar hardness to that of supercooled ice) showed a degree of ejecta collimation. These simulations included a second body, analogous to a second stage following the penetrator, interacting with the collimated ejecta plume.

1.3 Scope of Study

This thesis is a study of the creation and characterization of local transient atmospheres on icy bodies through the use of kinetic penetrators for the purpose of providing a medium through which a payload can interact and decelerate. This is a complex and multi-faceted problem. Involved is a detailed exploration of the mechanics of ice, hypervelocity impacts, aerodynamics, and numerical modeling. A review of the dynamics of ice will be presented with an accompanying methodology for modeling high-strain rate phenomena associated with shock-loading ice. The results from the modeling of the presented methodology will be extended to kilometer-scale events which will be used as the basis for parametric design studies of 'cryo'-braked Europan probes.

The emphasis of this thesis is on the methodology and tools created and used to formulate and attack the engineering problem presented. The results are meant to showcase the capability of the tools created and methodology used and to provide general trends of the studied phenomena, not necessarily as design parameters or conditions for mission development or planning. This sentiment is extended to the parametric studies of plume-probe interactions (presented in Chapter 4).

For clarity, the terms 'cryo-braking' and 'ejecta-braking' in this context both refer to using a plume of ejected ice, in any thermodynamic phase, as the medium through which drag can be created. These terms are used interchangeably in this thesis.

Chapter 2

Survey of Ice Energetics

The interaction of ice with structures is a driving design condition for many engineered systems, from ice ingestion of turbofan engines to hail impact of wind turbine blades to the cracking of ice sheets by an icebreaker's hull. In each of these scenarios, a battle between an engineered structure and nature is waged. Fortunately, engineers have developed the methods necessary to establish some sense of reliability and robustness for these systems despite the overwhelming uncertainty and variability of these discrete events. The physics behind these events are governed by very different principles. Examine the speed scales associated with these examples. A jetliner may be traveling upwards of 500 miles per hour (about 225 meters per second). The tip speed of a wind turbine blade may be in excess of 180 miles per hour (about 80 meters per second). On the other hand, an icebreaker might be lucky to exceed a walking pace (roughly 3 miles per hour or 1.35 meters per second). Knowing that kinetic energy is proportional to the square of velocity, the kinetic energy per unit mass of the ice ingestion of the jetliner is more than 27,000 times that of the icebreaker's work. This large energy difference migrates the loading established from a slow compaction and cracking of ice-icebreaker interactions to very high strain rate and shock-loading characterized physics behind ice ingestion or impacts.

The present study deals primarily with hypervelocty impacts into ice. However, a review of mechanics and modeling of ice in all strain rate regimes is required, since kinetic penetrators experience all ranges of strain rate behavior (they do eventually stop and have zero kinetic energy).

2.1 Strength Properties

The mechanical and engineering properties of ice are derived from its microstructure and thermodynamics. Of interest are the parameters and properties of ice that dictate the bulk strength and compressive failure (a rate-dependent property). A high-level review of these properties is presented here, not as a comprehensive summary of the mechanics of ice, but rather as a distillation of what is required for the subsequent modeling efforts. The majority of the information regarding the mechanics of ice comes from Schulson's [2] featured overview of ice properties appearing in the Journal of Minerals, Metals, and Materials. Schulson's review paper has served as a starting point for several follow-on papers on the mechanics of ice under various loading conditions, from geophysical to ballistic. We are of course interested in the latter. Of note is that 'ice' itself is a misnomer, often referring to any of the 15 states 'ice' can take. The 'ice' in this study is assumed to be ice Ih since it is mechanically the strongest phase [2] and occurs at surface pressures.

As an elastic material, the bulk modulus of ice varies significantly as a function of temperature [2]. In addition, the elastic properties of ice are very dependent on the grain structure and orientation (uniaxial strength in the dominant direction of grains can greatly exceed bulk properties of ice by up to 40% [2]). For the sake of the engineering problem, the ice in this study is assumed to have a grain structure of perfectly random orientations. The properties of the ice are therefore independent of orientation or loading direction. The bulk loading modulus is taken to be 9.0 MPa with a Poisson's ratio of 0.33 [2].

The loading expected in hyper-velocity impacts is not elastic. However, the modeled

domain will include far-field ice that will not be shock loaded or perturbed to the point of failure. In these regimes, the response of the ice to the loading will fall on the elastic loading-unloading stress-strain curve. For the sake of capturing accurate pressure wave propagation in the ice, these elastic parameters are still important.

2.2 Failure Behavior

Figure 2.1 shows trends in the stress-strain curve in response to loading of different strain rates [2]. Slow or quasi-static loading (curve I) of ice exhibits ductile behavior in both compression and in tension. Contrasting this behavior, for high strain rate loading (curves III), the failure mechanism transitions to a brittle mode. Quantified, freshwater 'strong' ice follows the trend visualized in Figure 2.2. Of note is the peak in the developed mechanical stress as a function of strain rate. The behavior of compressive brittle failure will dictate much of the response in the hypervelocity impact modeling. Schulson [2] remarks of the effect of confinement (deviatoric) on observed strength of compressive loading (until the point of failure). Implied is the presence of slip planes along which cracks can propagate (should defects already exist in the ice).

The compressive failure mechanism transitions from ductile to brittle at strain rates on the order of $10^{-3}s^{-1}$ for 'cold' ice Ih. Figure 2.2 shows the uniaxial compressive failure surface as a function of strain rate. The failure stress state for high strain rates ($10^{-3}s^{-1}$) is nearly 10 times that of low strain rates. For hypervelocity impacts, it is essential that this phenomenon is adequately captured.

2.3 Hydrocode Material Models

The engineering and material science behind the wide range of physical behaviors of ice needs to be condensed into a usable form for a hydrocode. For the hydrocodes used,

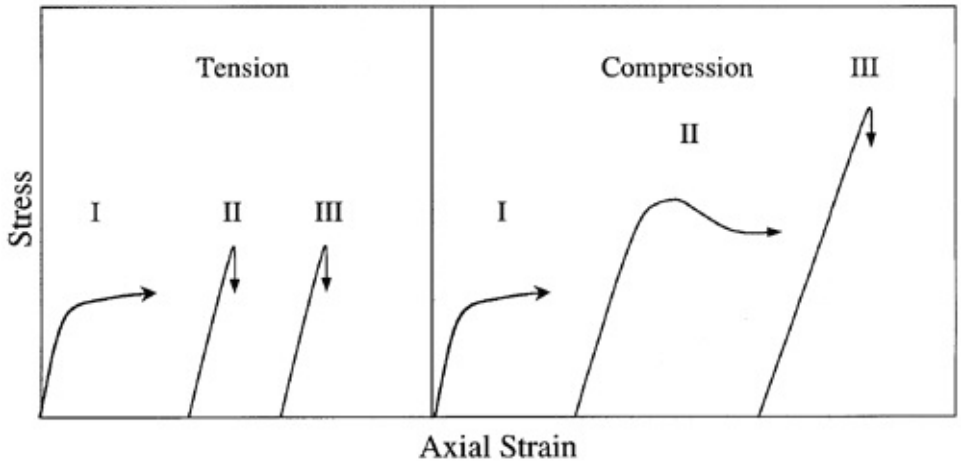

Figure 2.1: Transition of ice from ductile to brittle failure modes. I corresponds to low strain rate loading while III corresponds to high strain rate loading. Image reproduced from Schulson [2].

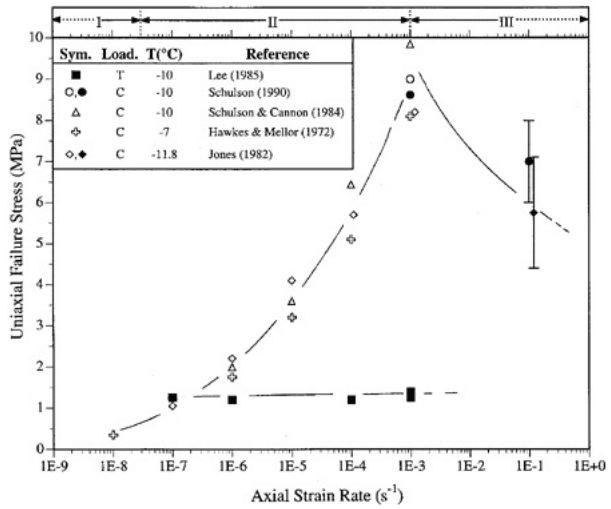

Figure 2.2: Influence of strain rate on uniaxial failure stress of fresh ice. Image reproduced from Schulson [2].

LS-DYNA and AUTODYN, validated ice material models from literature are used that capture the aforementioned physics.

Carney et. al. [5] underwent the task of creating a validated material model in the study of impacts of ice into space shuttle vehicles with high strain rate loading in 2006. Carney's ice material model is strain rate dependent, captures failure, experimentally validated, and easily implemented into the hydrocode LS-DYNA. The material model created follows closely experimental ballistic tests and is comprised of directly measured constants, making this material model very attractive.

ANSYS AUTODYN does not employ the same material model specifications as LS-DYNA, hence a different *experimentally validated* material model for ice from literature is used for AUTODYN. Kim and Kedward [4] performed a study of modeling hail ice impacts into various structures at high speeds. This study features a material model created from a hail cannon experimental program developed specifically for SPH codes (DYNA3D and AUTODYN). Fluid-structure contact behavior for high strain rate processes is used as a validation parameter for this study - a parameter that is critical for the presented research.

Each of these material models is summarized in Appendix A for convenience.

Chapter 3

Impact and Ejecta Modeling

The computational modeling effort is divided into two sections. The first section is the modeling of the experimental ice impact program at the University of Washington Ram Accelerator Laboratory. This section is to validate and verify the modeling techniques used in this study. The goal is that the results from the modeling of these smaller-scale experiments will provide necessary confidence in the latter section: modeling impacts and ejecta on a significantly larger scale for which no experiments are possible.

Modeling high energy and high strain rate phenomena is a multi-faceted (and multidisciplinary) task. A suitable computational formulation (and code that supports the formulation) must be adapted to the desired problem. The physical and computational spaces need to be well defined. The materials for the involved components must also be accurately modeled. Lastly, because ejecta behavior is dependent on boundary conditions of the physical domain, these must be understood and properly prescribed for the modeling.

3.1 Analysis Approach

For typical quasi-static structural engineering problems, the tool of choice is the classical finite element model. When applied properly, the underlying physics of the structure or system can be examined readily with modest computational effort. Most finite element problems are linear and solved implicitly, meaning through matrix inversion and manipulation. For fast, energetic phenomena involving inertia (that are more often than not also highly non-linear), the implicit formulation for finite elements breaks down because of numerical instabilities requiring an ever-decreasing timestep. Explicit formulations for finite elements exist in many commercial codes for such problems. Explicit formulations use phase and group velocity of waves developed in the discretized medium to dictate the progression of the model. The solution procedure is formulaic and only needs to be calculated once per timestep, unlike implicit analyses which are iterative in nature. The solution procedure is based off of the solution of conservation equations rather than a set of matrix equations. For this reason, explicit analysis codes are often referred to as *hydrocodes*. The discretization and formulation of the conservation equations vary widely depending on the intended application and physics involved.

3.2 Computational Formulation

All models considered here are constructed as two-dimensional axisymmetric. This significantly reduces the size and computational cost of the model. Off-axis penetration tests are therefore not possible with this specific analysis, but the presented formulation can be extended to three dimensions should off-axis cases need to be examined.

Several options exist for the discretization of the computational domain. The most straightforward approach is the use of a simple Lagrangian mesh. This method approximates the solids of the problem, the penetrator and ice, as a set of connected elements that move with the prescribed motion of the body. Complications arise from this

formulation when the deformation of the body becomes excessive. In any computational physics method, the analysis can and will fail from numerical instabilities if Lagrangian elements become too skewed or self-intersect. For problems in which large deformations are expected, great care must be taken to ensure the robustness of a Lagrangian mesh. This might include creating a structured mesh or strongly biased mesh (biased towards the regions and directions of expected deformations).

The penetrators for this study are modeled in a Lagrangian fashion. The expectation is that the penetrators deform outward (by design), much like the mushrooming of a rivet. The mesh is laid out such that after deformation the elements are still of good quality and not excessively skewed. This is an iterative process. Figure 3.1 shows an example penetrator mesh at time zero. Figure 3.2 shows an example of a post-loading deformation. While the overall shape of the penetrator has changed dramatically, the quality of the mesh has remained in tact and can be fully resolved.

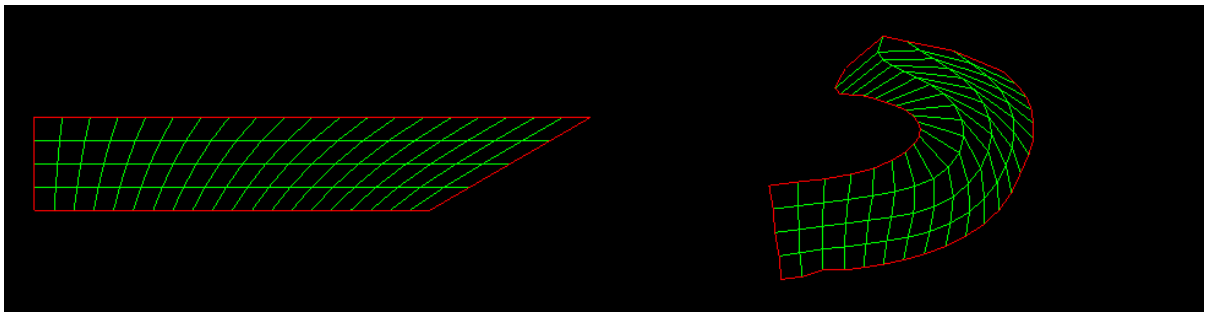

Figure 3.1: Axisymmetric mesh.

Figure 3.2: Mesh after deformation.

Because the ejecta and fluid-like behavior of ice at high strain rates are of interest, the ice is not modeled with a Lagrangian mesh in areas of large deformation. Two alternative approaches are explored: Smoothed Particle Hydrodynamics (SPH) and the Arbitrary Lagrangian-Eulerian (ALE) formulation. These formulations are discussed within the context of the hydrocodes AUTODYN and LS-DYNA, respectively. The governing conservation equations for each formulation are presented.

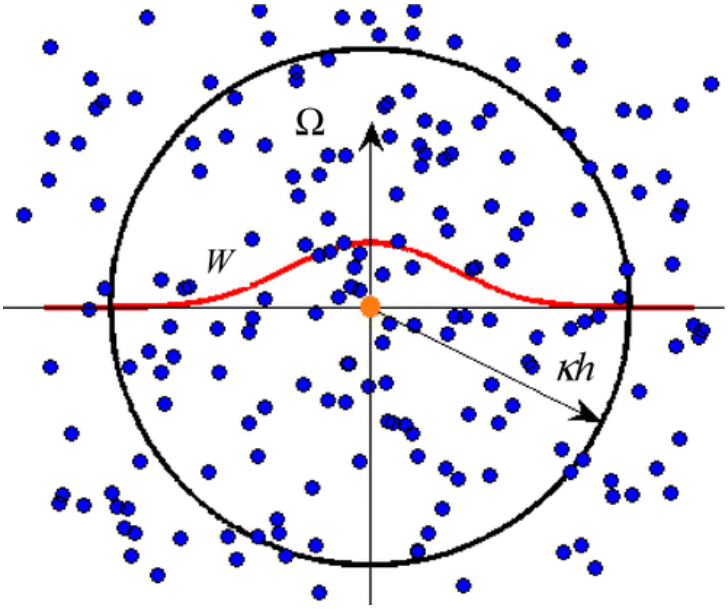

Figure 3.3: An example smoothing kernel and particles of the Smoothed Particle Hydrodynamics method [3].

3.2.1 Smoothed Particle Hydrodynamics

Smoothed Particle Hydrodynamics is a Lagrangian-type formulation in which the continuous material is modeled as a set of discrete particles. Each particle is assigned a mass and can react to mechanical loads in accordance to the smoothing function, or kernel, of the formulation [3]. The kernel function, a pictorial example of which is shown in Figure 3.3, smooths the properties of the continuous medium within the smoothing length of the formulation (smoothing length is a parameter chosen by the user depending on the number of particle neighbors, which is typically held constant).

As a particle-tracking technique, the method is mesh-free. This is an incredible asset for problems with extreme deformations, since the smoothing kernel dictates the calculation and update of the properties, not the domain of a Lagrangian mesh. Because of the importance of the production and behavior of ejecta after penetrator impact, the SPH technique is an attractive computational option. The mesh-free nature of the formulation has no restrictions on domain because the ejected particles can travel in space without constraint.

SPH Form of Conservation Laws

In the particle tracking scheme, the behavior of each of the particles is computed from the solution of the conservation of momentum and energy applied to the ith particle [14]. Note that conservation of mass is inherited implicitly through the formulation.

$$\frac{d\mathbf{v}_i}{dt} = \mathbf{a}_i^P + \mathbf{a}_i^{visc} - \nabla\Phi_i \tag{3.1}$$

$$\frac{du_i}{dt} = \frac{P_i}{\rho_i^2}\frac{d\rho_i}{dt} + H_i \tag{3.2}$$

In these equations, the gravitational potential is manifested through Φ, u is the specific internal energy, H is the power difference for non-adiabatic processes, and $\mathbf{a}$ are the accelerations due to pressure, P, and viscous forces.

The pressure acceleration term and the derivative of scalar properties are functions of the smoothing kernel $W(r, h)$, where r is the distance between particles and h is the kernel smoothing length. These relationships are not reproduced here, but noted is the complete set of equations in [14].

AUTODYN SPH Setup

The implementation of 2D axisymmetric SPH in AUTODYN is straightforward. The fluid-structure interaction algorithms ('fluid' being the SPH particles and the 'structure' being the penetrator) are applied automatically by detection, eliminating the need for prescription of master and slave nodes.

Convergence of the model was achieved by increasing the number density of the SPH domain until a quantitative result (typically deceleration profile of the penetrator) did not deviate by more than 5% of a more coarse model. For most models, this translated to roughly 8 SPH particles within the throat of the hollow penetrator. All presented results in this study were sized according to this procedure.

Ejecta Plume Formulation

Particle tracking comes with a unique set of challenges for ejecta modeling. The smoothing length of the kernel function is typically set by the user (or as a computed default from the hydrocode) corresponding to the number density of the particles over the initial physical domain of the SPH part. For modeling ejecta over large time spans, the divergence of the ejecta plume implies a loss of smoothing in later time steps. This biases the solution field towards a field of discrete particles rather than a smoothed field of continuous ice ejecta. This isn't necessarily a problem except that the particles are all of fixed mass, which restricts the density of the plume if no neighbors are within the smoothing length for any given particle. Density of the plume for times on the order of seconds requires a variable smoothing length and projection of the density onto a meshgrid-like data structure.

To exemplify these characteristics, several example models were built and run in the Ansys in-house hydrocode AUTODYN (as opposed to LS-DYNA; AUTODYN exhibits better stability for 2-D axisymmetric hypervelocity impact models). This immediate example model is for demonstration purposes only.

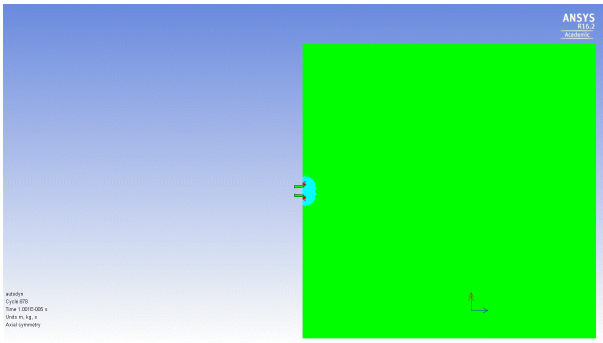

Figure 3.4: SPH Impact; $t = 1.0 \cdot 10^{-5}$ s.

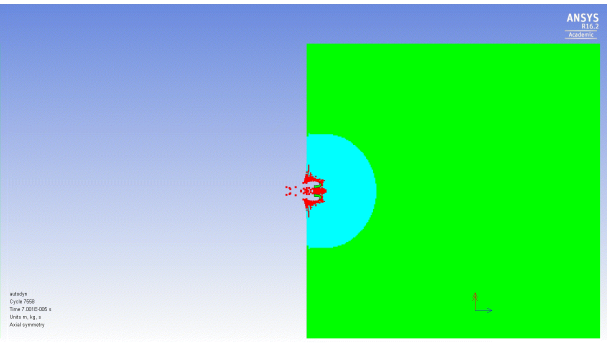

Figure 3.5: SPH Impact; $t = 7.0 \cdot 10^{-5}$ s.

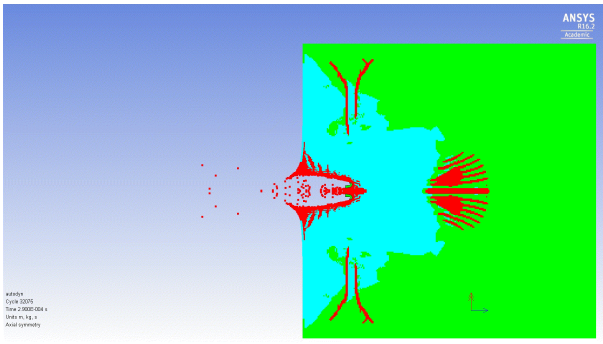

Figure 3.6: SPH Impact; $t = 2.9 \cdot 10^{-4}$ s.

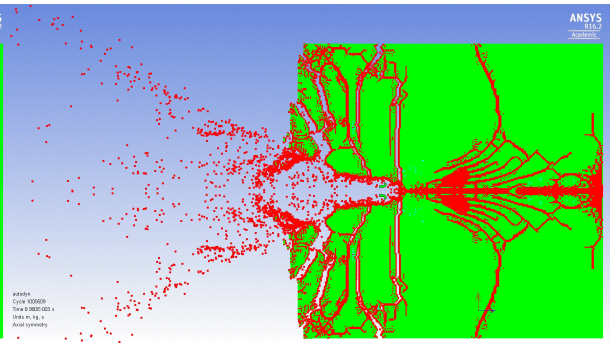

Figure 3.7: SPH Impact; $t = 8.98 \cdot 10^{-3}$ s.

Figures 3.4 through 3.7 show a hollow cylinder penetration (1 km/s) into a block of ice modeled of SPH particles. The red particles are those that have been flagged as having been mechanically loaded past ultimate strength (mechanical failure), blue are those undergoing plastic deformation (there is a degree of re-heal implemented in the model), and green is in the elastic region. The model is 2D axisymmetric and constrained along the side and rear faces. For this test case, the physical dimensions and quantities are not of critical importance. However, a critical parameter that should be highlighted is the number density of the SPH particles relative to the size of the penetrator. For this model, there were at least eight particles (in the undeformed state) across the throat of the penetrator. This was found to be the limit for sizing the domain and particles in a convergence study.

There are two options for recasting the discrete particles into an effective 'atmospheric plume'. The first option is to take the plume to be exactly what is shown in the results of the SPH models - a collection of discrete ice pieces of fixed mass that are fundamentally independent. This is analogous to free-molecular flow. Interactions with the plume would need to be modeled as a set of individual collisions through which momentum and energy would be transferred. The second option is to post-process the discrete particles in a way that portrays them as an *effective* plume.

The first method is arguably the most accurate method for plume interaction, though this is the most computationally-intense (and prohibitive). Computational runs out to

20 or even 30 seconds could take years to complete on single-threaded programs like AUTODYN in 2D. Also, it could be expected that late into the ejection process the SPH method and subsequent plume characterization may give non-realistic interactions with other ice particles or 'third bodies' that may be involved. This effect is because of the loss of number density of the particles for times long after impact (greater than 10 ms or so). To truly capture the physics with particle collision tracking, the number density would have to be large enough to be significant at kilometer scales. The initial ice domain into which the penetrator strikes is on the order of meters.

The second method requires significant post processing. An 'effective density' needs to be derived from the SPH discrete particle field. To do this, a post-processing program was made to convert the SPH particle field into a continuous density plume. The program's methodology is quite simple. First, the SPH particles are split into a large number of sub-particles, each with a fraction of the original particle's mass. This splitting process is driven by the conservation of momentum, but does not balance the thermodynamic energy equation. The particle splitting routine assigns random velocities to the new particles until the total momentum before and after splitting is the same. In this manner, the number density of the plume is greatly increased and the plume becomes more continuous. To smooth the plume over the domain of interest (on the order of kilometers), a meshgrid structure in MATLAB is initialized as a physical/computational domain on which the density of the plume can reside. A 'nearest neighbor' algorithm searches for particles (which have been split from the original SPH particles) as the program loops through the meshgrid indices, populating the meshgrid with an averaged value. This method smooths the ejecta plume based on the radius specified in the 'nearest neighbor' search routine. This method by which the plume is created is a consistent with kernel smoothing used by commercial SPH codes, but because of the assumption of free molecular flow, the energy equation can be neglected.

Figure 3.8 displays the axisymmetric portion of the ejecta plume after post-processing from the impact pictured in Figures 3.4 to 3.7. This form is usable in the calculation of

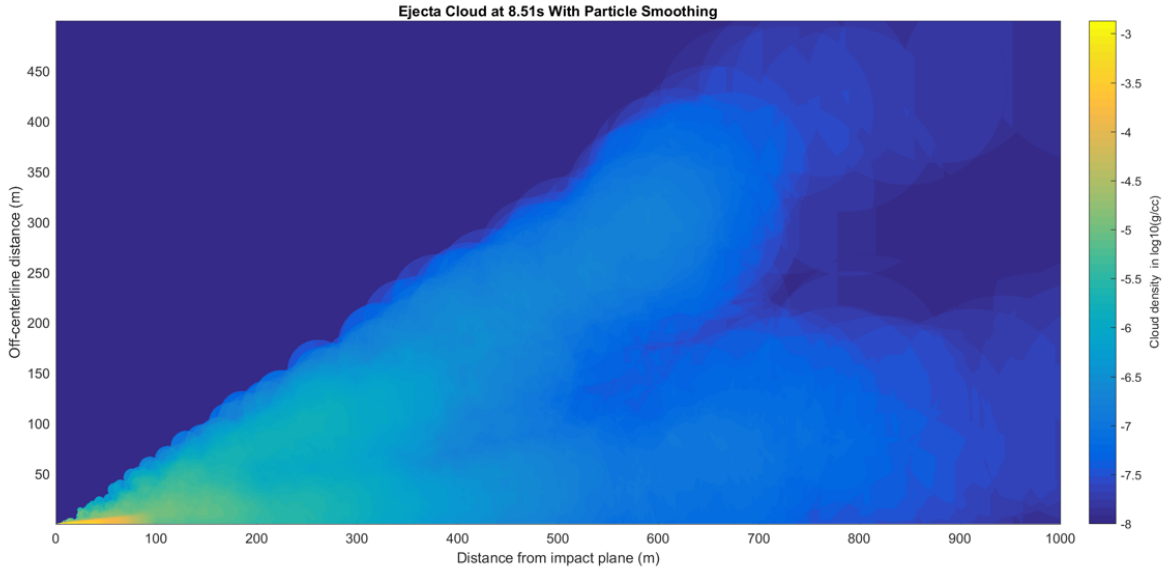

Figure 3.8: Axisymmetric smoothed plume from AUTODYN SPH results post-processing particle splitting routine.

drag for probes of arbitrary shapes and mass properties detailed in Section 4.1.

3.2.2 Arbitrary Lagrangian-Eulerian Techniques

Arbitrary Lagrangian-Eulerian (ALE) refers to a set of techniques that combine some features of Eulerian-type meshes with the conventions of Lagrangian formulations. The ice for ALE models is set as an Eulerian domain through which ice is initialized and can flow between elements. This enables the model to respond to very high levels of deformation and energy input without the need to re-mesh a Lagrangian structure. Numerically, this is a type of volume-of-fluid computational fluid dynamics (CFD) formulation in which the interface of the advected material or fluid is tracked and reconstructed on the Eulerian domain [15].

The method is said to be 'arbitrary' in that the nodes of the Eulerian mesh are allowed to move through space should the physics dictate the motion is necessary. For example, consider a partially filled water bottle that is thrown. In an ALE formulation, the inside of the water would be modeled as an Eulerian mesh upon which the fluid (water)

would be initialized and could flow. The water could then interact with its surroundings (the bottle, which would be modeled as a Lagrangian structure) through fluid-structure coupling constraints. The bottle itself has motion - meaning that the Lagrangian and Eulerian meshes both move in absolute space. In this manner, the Eulerian mesh is said to be *arbitrary*. Secondly, when the bottle inevitably impacts the ground, the bottle may deform, meaning that there may exist relative displacements (and therefore motion) between the bottle and the Eulerian mesh. This local motion also contributes to the uniqueness of the ALE method.

Suppose the water bottle in this thought experiment contained two or more fluids. The ALE technique, now multi-material ALE (or MMALE), tracks the interfaces of the materials within the Eulerian domain as the materials advect. The properties at a given location in the Eulerian domain is taken to be a weighted average of those of the different materials.

For the penetration and ejection of ice, the ice is modeled as a fluid that is initialized on a purely Eulerian domain. For these studies, the Eulerian mesh does not move with the material. The modeling approach is identical to conventional MMALE models with the exception of boundary and initial conditions on the Eulerian domain. Because there is no desire for the mesh to move, the problem is cast as a typical computational fluid dynamics problem (solving conservation equations). This treatment allows for the flexibility to characterize and extend the ejecta plume in ways that are not immediately possible with SPH methods.

ALE Form of Conservation Laws

Beginning with the differential forms for the conservation laws (listed below as mass, momentum, and energy, respectively), the bulk motion can be included in the velocity terms to update locations [15]:

$$\frac{d\rho}{dt} = -\rho \boldsymbol{\nabla} \cdot \mathbf{u} \tag{3.3}$$

$$\rho \frac{d\mathbf{u}}{dt} = \boldsymbol{\nabla} \cdot \boldsymbol{\sigma} + \rho \mathbf{b} \tag{3.4}$$

$$\rho \frac{dE}{dt} = \boldsymbol{\nabla} \left(\boldsymbol{\sigma} \cdot \mathbf{u} \right) + \mathbf{u} \cdot \rho \mathbf{b} \tag{3.5}$$

In these equations, ρ is the density, $\mathbf{b}$ is an arbitrary body force, such as gravity, and E is the specific total energy. Two alterations need to be made to recast the conservation equations to structural problems. The first is to rewrite the energy equation in terms of specific internal energy:

$$\rho \frac{de}{dt} = \boldsymbol{\sigma} \mathbf{:} \boldsymbol{\nabla}^S \mathbf{u} \tag{3.6}$$

where the right hand side describes the strain rate effects of the material on the internal energy. This is critical for materials modeled with equations of state with strain rate dependencies, such as in the presented case [5]. The second modification is the inclusion of bulk motion in the velocity term. Define the convective velocity:

$$\mathbf{c} = \mathbf{u} - \hat{\mathbf{u}} \tag{3.7}$$

where $\hat{\mathbf{u}}$ is the bulk velocity in absolute space of the host or mesh. The differential form of the conservation equations for ALE come after substitution of the convective velocity:

$$\left. \frac{\partial \rho}{\partial t} \right|_{\boldsymbol{\chi}} + \mathbf{c} \cdot \boldsymbol{\nabla} \rho = -\rho \boldsymbol{\nabla} \cdot \mathbf{u} \tag{3.8}$$

$$\rho\left(\left.\frac{\partial \mathbf{u}}{\partial t}\right|_{\boldsymbol{\chi}} + (\mathbf{c}\cdot\boldsymbol{\nabla})\,\mathbf{u}\right) = \boldsymbol{\nabla}\cdot\boldsymbol{\sigma} + \rho\mathbf{b} \tag{3.9}$$

$$\rho\left(\left.\frac{\partial e}{\partial t}\right|_{\boldsymbol{\chi}} + \mathbf{c}\cdot\boldsymbol{\nabla}e\right) = \boldsymbol{\sigma}\!:\!\boldsymbol{\nabla}^{S}\mathbf{u} \tag{3.10}$$

Again, equations 3.8 through 3.10 are the mass, momentum, and energy equations, respectively. In this notation, $\boldsymbol{\chi}$ denotes absolute space or an absolute reference frame. Purely Eulerian and purely Lagrangian forms can be recovered from these equations by setting $\hat{\mathbf{u}} = 0$ or $\hat{\mathbf{u}} = \mathbf{u}$, respectively [15].

LS-DYNA Multi-Material Arbitrary Lagrangian-Eulerian Setup

There exist several different options for constructing and setting up the Multi-Material Arbitrary Lagrangian-Eulerian (MMALE) model in LS-DYNA. The specific considerations and specifications are summarized here.

Reference Frame

The ice is modeled in a purely-Eulerian fashion. The mesh has no motion and the convective velocity is equivalent to the material velocity. This still falls within the ALE class of models since the solver and treatment of fluid-structure coupling are identical. Choosing a purely Eulerian framework with which to work has severe consequences. This is no longer a mesh-free technique like SPH - the physical domain must be specified in the model setup. The domain is incredibly restrictive for this reason. However, the flexibility gained by the portrayal of the ejecta plume as a continuous field opens up post-processing opportunities that allow one to bypass the physical restriction of the Eulerian mesh. If an expanding mesh was chosen instead of a purely Eulerian mesh, the mesh would become distorted in later times as the formulation attempts to uphold the conservation of mass within its boundaries. This will artificially smooth and corrupt the plume shape and

density (since the physical quantities are dependent on cell area, and the growth of that area is unchecked as the run time increases).

Numerical Solver and Specifications

LS-DYNA supports several different solvers for the ALE method. Each has specific uses, pros, and cons. In general, the models constructed and presented here are solved with a second-order accurate Van Leer half shift solver. This is the highest-order solver for the ALE method implemented in LS-DYNA. Two first order methods are available, but are not used for anything but convergence studies. The first order solvers are markedly faster (wall time), though the monotonicity of the numerical scheme may not be preserved [16]. Artificial damping of these schemes may improve the numerical properties, but in order to avoid adding more variables to the mix, the highest-order scheme available was used.

Fluid-Structure Interaction

Because the ice is modeled as a fluid, the interaction between the fluid and the structure (FSI) needs to be specified. The 'structure' in this sense is defined as a Lagrangian-modeled solid - the penetrators. LS-DYNA handles FSI for MMALE simulations through a constraint input card with options for treatment of interfacial loads. Numerically, this interaction is handled by splitting the elements of the Eulerian domain into a number of sections or zones (defined by the number of quadrature points). LS-DYNA checks the penetration of the Lagrangian structure into the Eulerian domain based on the resolution and zoning defined by these quadrature points. This is chosen to be four for this study - a trade-off between penetration resolution and computational load.

The choice also exists for coupling of materials. Explicit specification of coupling groups is useful if one or more of the multi-material groups does not contribute significantly to the loading of the Lagrangian structure. For example, the vacuum material in these

simulations are necessarily included in the models to occupy space, but the vacuum material will not affect the loading on the penetrator. Likewise, if the geophysical domain is stratified or some areas may not influence the immediate loading of the penetrator, these can be excluded from the coupling constraint. The benefit is computational efficiency. LS-DYNA will not have to probe all locations of all materials to check for penetration - only the locations of the material groups of interest.

The coupling constraint can be handled one of two ways. In the default constraint setup, the solver simply checks penetration based on the quadrature point specification and adjusts the Eulerian domain's contents such that the Lagrangian structure and Eulerian materials do not occupy the same space. For most problems, this constraint setup is acceptable. However, for specification of interaction of shell elements or extreme loading, leakage may occur where the Eulerian material passes through the Lagrangian structure (non-physical). To get around the leakage issue, control over the interface pressure can be given to the user as a pressure coupling curve. The definition of this curve is somewhat iterative. In a simulation with standard coupling with leakage, the pressure at which leakage occurs is taken to be the maximum contact pressure. A bi-linear curve (Figure 3.9) can then be defined that specifies the interface pressure as a function of penetration depth. For the initial ramp, the pressure goes from zero (no penetration) to P_{max} at 10% penetration (based on normal projection length D of a Lagrangian node onto an edge of an Eulerian element of edge length L). This coupling pressure is then held constant with increasing penetration depth. In implementing this leakage control scheme for the first time, the maximum pressure in the Eulerian domain may change, hence the iterative process for prescription of P_{max}.

Mesh Tolerance and Convergence

LSTC [16] recommends using an Eulerian mesh that is as fine or slightly finer than that of the Lagrangian structure for good FSI coupling. To illustrate why, consider two examples. Take an Eulerian mesh whos element size is larger than that of the Lagrangian

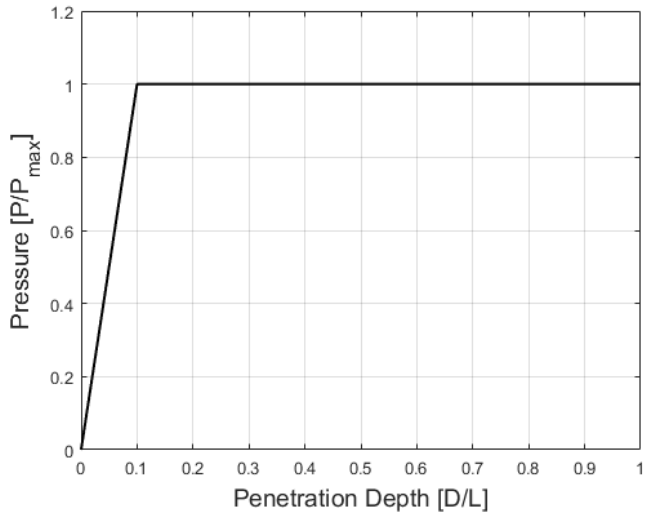

Figure 3.9: Coupling pressure for a given penetration depth of Lagrangian structure into Eulerian element of characteristic length L.

structure. In this scenario, the deformation of the Eulerian material is limited by the size of the Eulerian mesh. When the 'fluid' interface is reconstructed, if the Lagrangian structure is small in comparison, there will be no apparent deformation and significant leakage. On the opposite end of the spectrum, consider an Eulerian mesh whose elements are significantly finer than that of the Lagrangian structure. In this case, the loading on the structure has lost the detail of the interface conditions as these properties are effectively averaged between the nodes of the structure. Local pressures in some of the Eulerian cells could be orders of magnitude higher, but the local effects experienced by the structure are washed out because there is no nearby node to react the load. Having similarly sized meshes allows for the local effects to be 'experienced' while preserving a physical fluid structure interface.

The sizing of the meshes for both the MMALE and Lagrangian domains is limited on the deformation experienced by the penetrator. The elements of the penetrator must be small enough to capture the local plastic deformation ('peening') at the knife edges without becoming overly distorted or self-intersecting. It is worth mentioning that these characteristic deformations are critical in plume shape, since they form 'aerodynamic' surfaces to shape the ice as it travels through the penetrators. Arriving at a mesh that

is successful in displaying these physical characteristics is somewhat of an art - it takes significant iteration and experience to tune.

Immediately, this raises the issue of the computational size of the Eulerian domain, especially if the size of the domain needs to be sized to limit 'contamination' of pressure wave reflections off of boundary conditions. Again, this is a trade that must be studied. Because the formulation used immediately in this study is 2D axisymmetric, the penalty is not that great to keep constant mesh size (structured or unstructured) throughout the domain. In short, for 2D axisymmetric, this can be ignored. When moving to 3D, however, this becomes critical and may bring progress to a standstill.

3.3 Experimental Validation

An experimental program was developed [13] for the purpose of plume and crater characterization. The results from this effort are used to compare and contrast the SPH and MMALE impact models and to instill confidence in the reader of the validity of the formulations in ejecta plume modeling.

3.3.1 Apparatus and Target

The University of Washington Ram Accelerator Laboratory houses a 1.5" nominal bore Light Gas Gun (LGG) capable of propelling projectiles suitable for study of ice ejection and plume collimation.

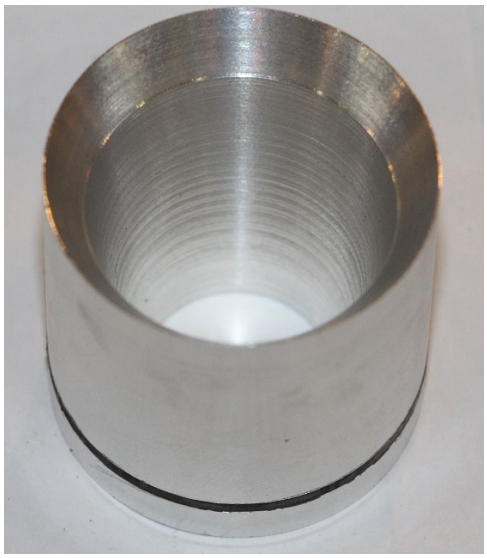

Figure 3.12: Example projectile used for LGG-capture plate experiments.

Figure 3.10: Ice target.

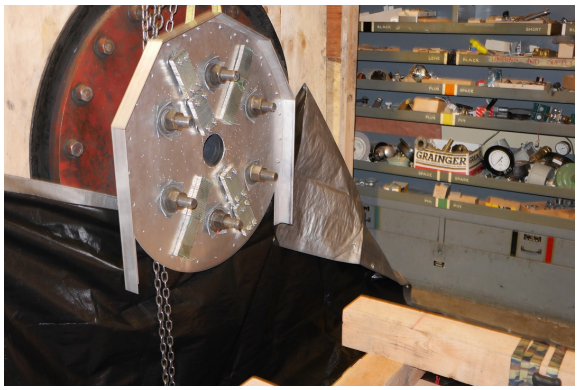

Figure 3.11: Capture plate for ice retrieval.

Figure 3.12 is a picture of one such hollow penetrator specifically designed to promote ejection and collimation of an ice plume. For this validation effort, a similar penetrator was shot into the ice target at high speeds. The ice target for this validation shot is pictured in Figure 3.10. It is important to note the several-inch thick layer of frozen sawdust-water energy attenuator about the ice core. This layer is important for preserving the target container as well as providing a more realistic (closer to a pseudo-infinite) boundary condition. The target is strapped down to its support in ambient (room temperature) conditions while the LGG is prepared. Figure 3.11 shows a capture plate used to test material durability under ejecta plume loading. The plate also directs ejected

Table 3.1: LGG Validation Shot

Parameter	Value	Description
Penetrator L/D	1	Ratio of length to diameter
Nominal OD	1.49 in	Diameter of penetrator
Nominal ID	1.0 in	Diameter of internal surface
Knifde edge angle	30°	Relative to centerline
Penetrator material	AL 6061-T6	Aluminum alloy used for penetrator
Penetrator mass	56.45 g	Penetrator mass only
Impact velocity	$1159\frac{m}{s}$	Estimated from high speed video
Target diameter	28 in	Diameter of ice target
Target depth	40 in	Depth of ice target

ice downward into a waiting container for later analysis.

For these shots a high frame rate camera is fixed on the impact plane to capture the penetrator as it enters the ice, as well as the immediate ejection and cratering processes. These high-speed camera images are the main source of data for model validation. Table 3.2 lists the complete specifications for the shot, which are then mirrored in modeling space with the SPH and MMALE models.

3.3.2 Experiment Results

Figures 3.13 and 3.14 show the crater of the target after impact and loose debris removal. The crater is shallow: roughly 6 inches in depth compared to the 28 inch diameter of the ice target. The crater also exhibits a great deal of spalling - significant surface eruption occured, so much so that a thick layer of ice was removed from target as ejecta (the depth of which is shown in the vertical red line in Figure 3.13). By assigning a representative density of $895\frac{kg}{m^3}$ (typical for progressively-frozen ice in ambient pressures), the ejected mass is estimated to be 29.9 kg (0.0335 m^3 of ice removed).

The high-speed video frames provide good estimates of the centerline ejecta speed as well as qualitative looks at the ejection and cratering processes. Figures 3.15 and 3.16 show the graphical extraction of velocities from the high-speed video frames. For this

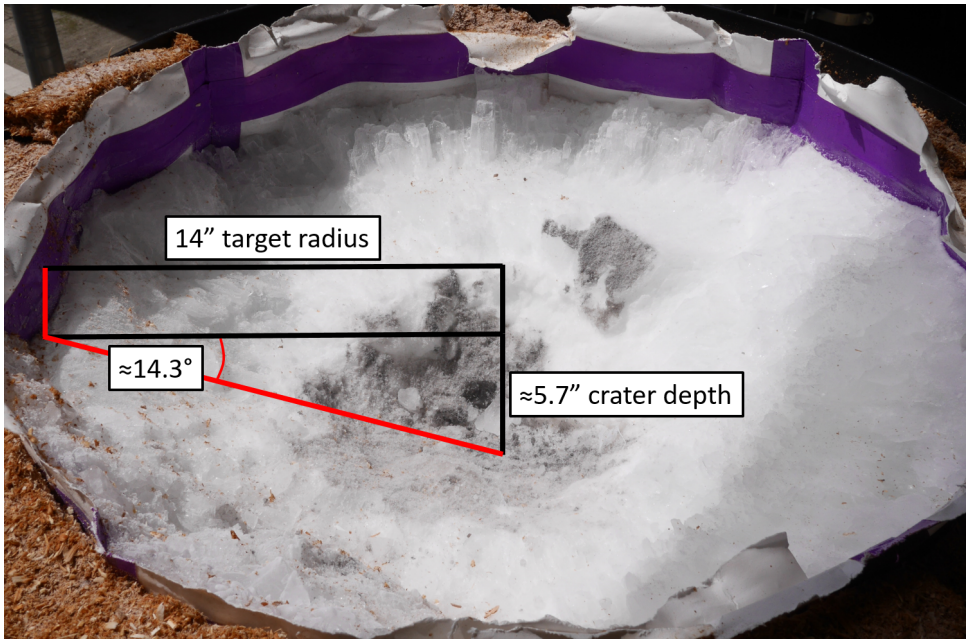

Figure 3.13: Shallow crater of laboratory hypervelocity impact.

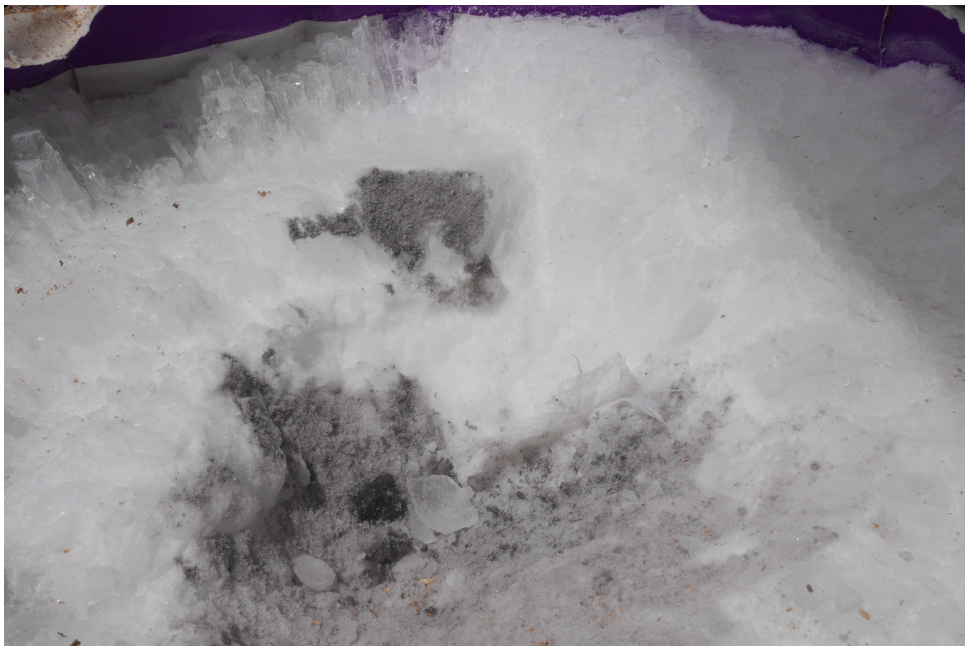

Figure 3.14: Ice failure surfaces and fragmentation post-impact.

experiment, the penetration velocity is 1160 m/s. The maximum centerline velocity of the ejecta plume is estimated, from Figure 3.16, to be about $545\frac{m}{s}$, or 47% that of the incoming velocity of the penetrator.

The surface eruption of the target during impact can be seen in Figure 3.17. The plume at this point extends beyond the field-of-view of the camera, but the camera still captures the ejection of the larger ice particles (very nearly 'chunks' at this point). Qualitatively, this material is consistent with the cylindrical ejected portion previously shown in Figure 3.13 - the failure surfaces imply larger pieces of ice being ejected in the periphery of the target.

3.3.3 Model Comparisons

The MMALE and SPH models of this impact are compared against the criteria listed in Table 3.2. Of these parameters, only the ejected velocity is a direct output of the solvers. The ejected volume is estimated graphically from the crater geometry, which is measured by the user in post.

SPH Validation Model

Figures 3.18 and 3.19 show the AUTODYN SPH model of the validation experiment. Although the number density of the particles is low for the initial collimated ejecta of ice in the model, the velocity of the collimated ejecta shown in Figure 3.18 is estimated to be $400\frac{m}{s}$. Likewise, the crater volume is estimated by drawing an 'ejection line' in a saturated velocity plot of the particles. Such a plot is shown in Figure 3.19, where the non-blue particles represent those which are moving in the direction of the ejection. The line bounding these particles gives a integratable surface from which volume can be extracted. Multiplying by the density of ice, the ejected mass is calculated to be 28.3 kg. Lastly, the penetration depth (or crater depth) is 6.6".

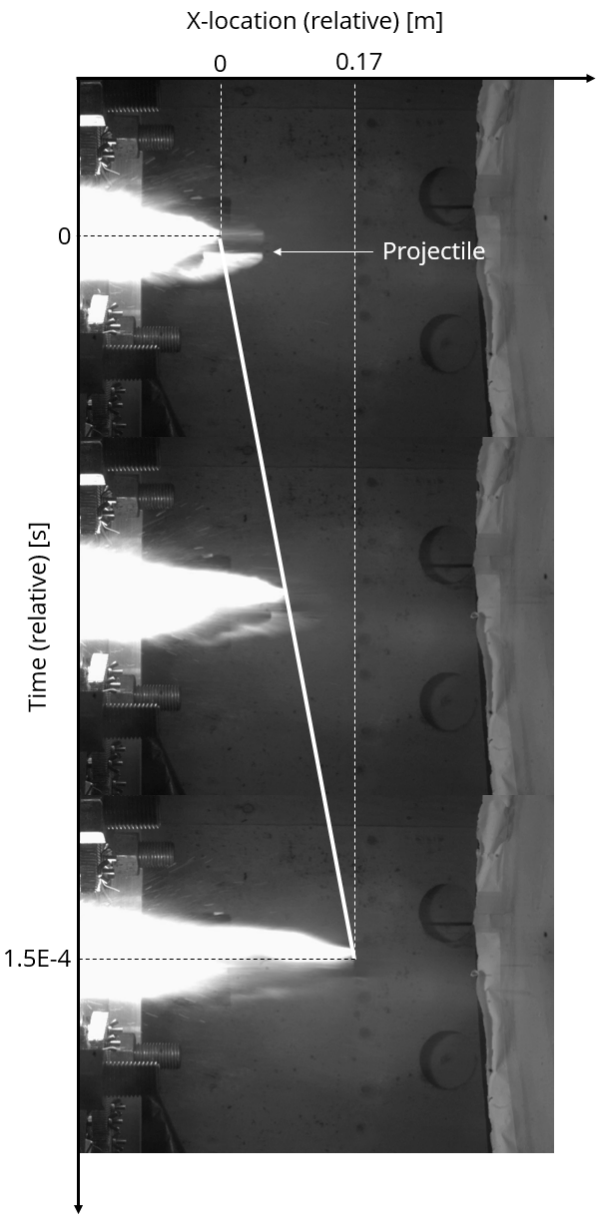

Figure 3.15: X-T of projectile.

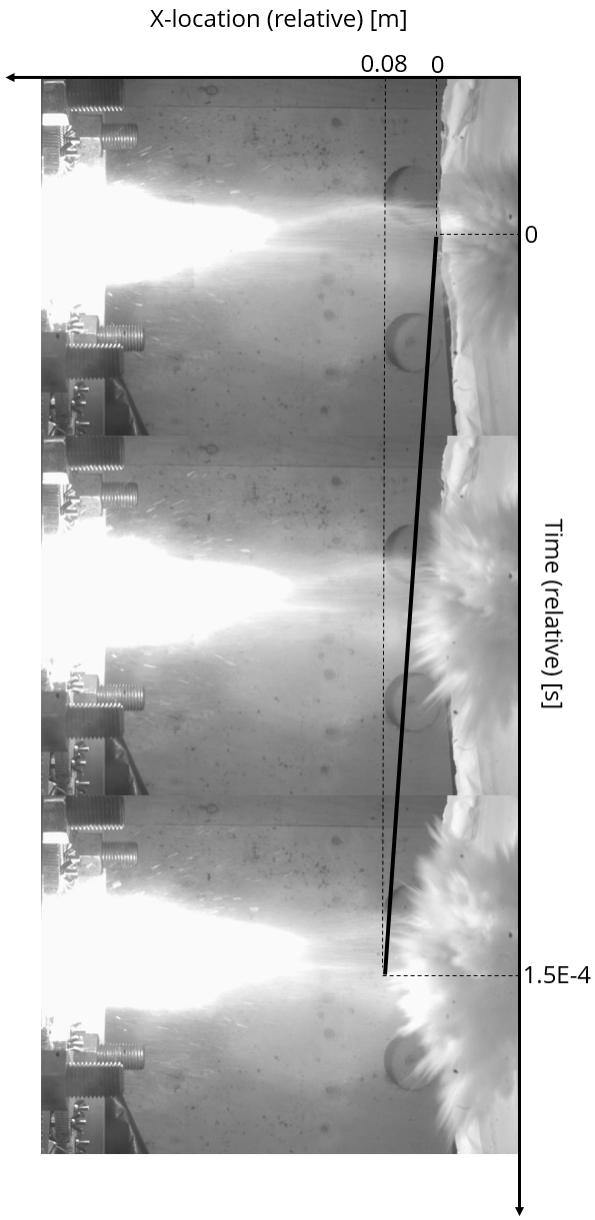

Figure 3.16: X-T of plume.

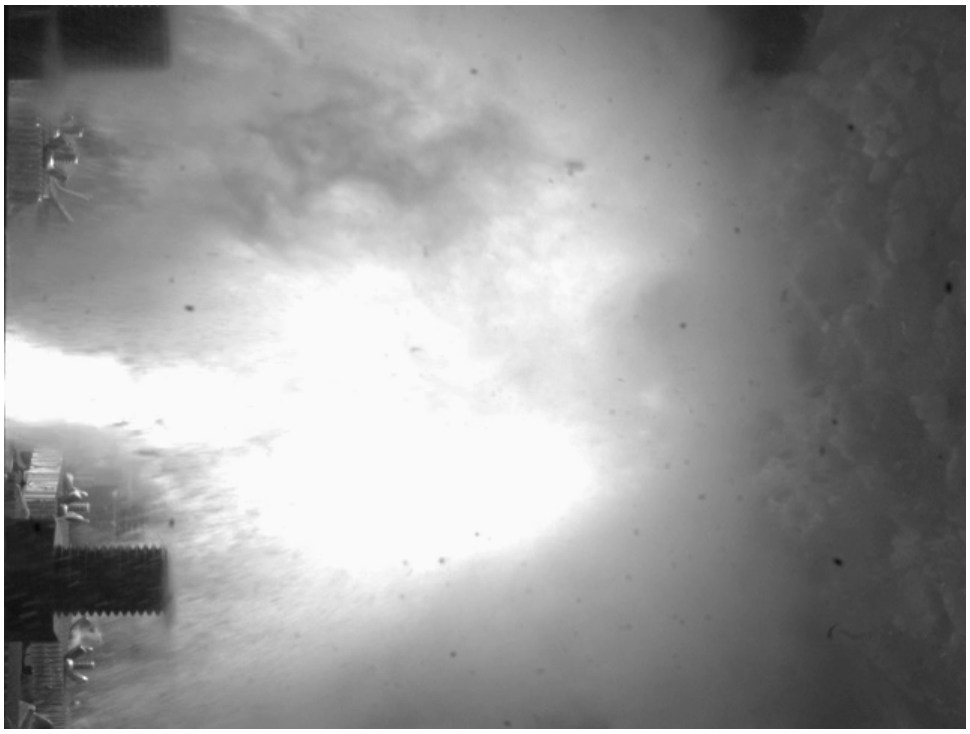

Figure 3.17: Target surface eruption during impact.

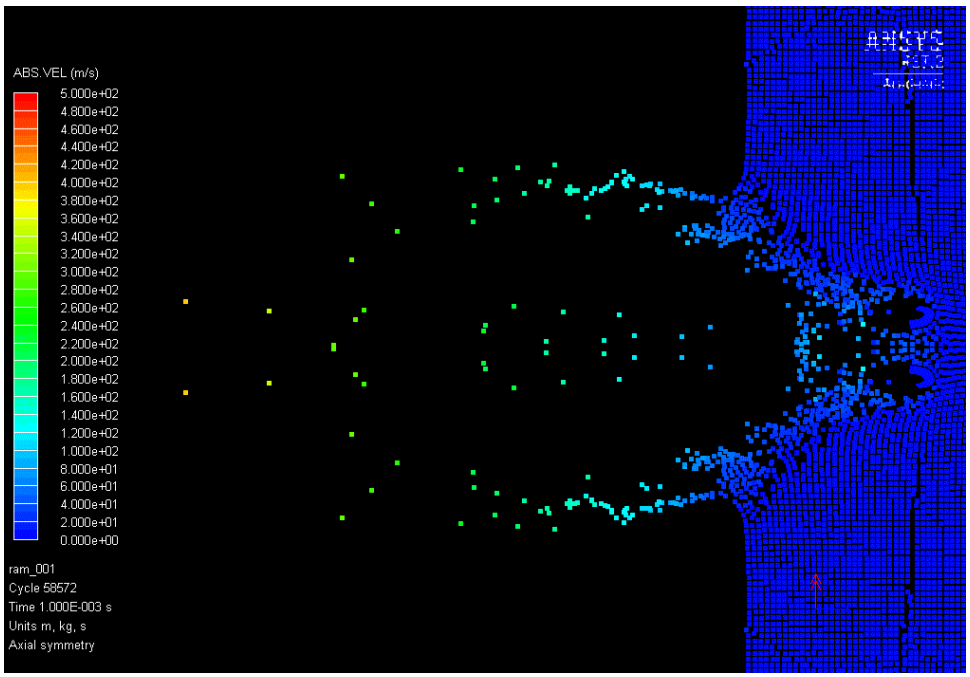

Figure 3.18: SPH early-time plume velocity.

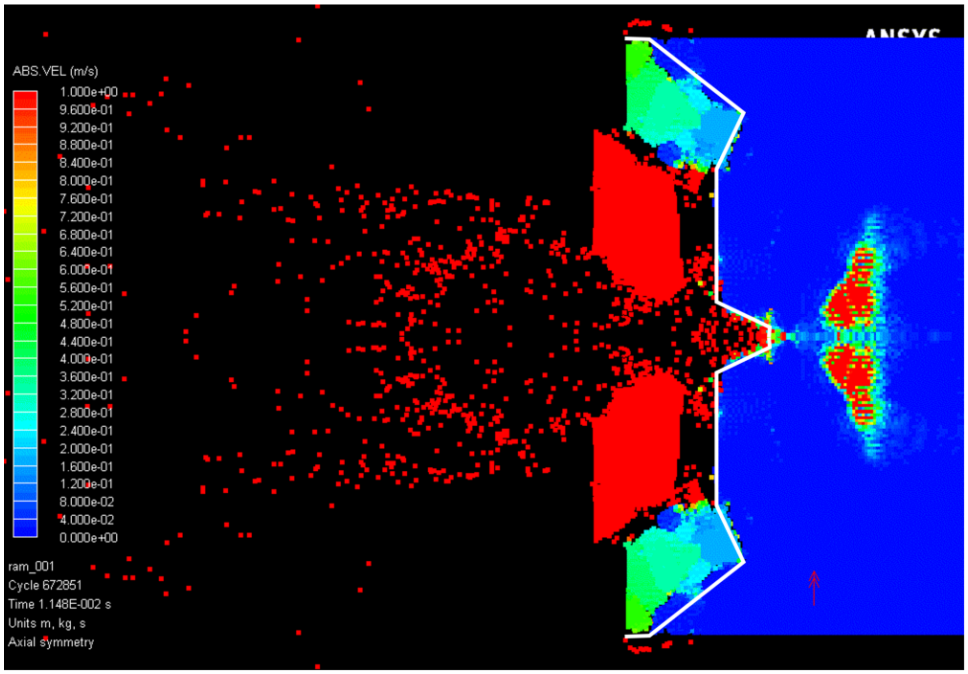

Figure 3.19: SPH ejection line.

MMALE Validation Model

Figures 3.20 and 3.21 show the LS-DYNA MMALE model of the validation experiment. Unlike the SPH formulation, MMALE relies on boundary reconstruction for the treatment of field variables, including velocities. As such, the collimated ejecta velocity is a direct output - 255 $\frac{m}{s}$ for the early-time snapshot shown in Figure 3.20. By lowering the saturation limit of the plots, one can easily discern what regions of material are included in the ejection region. The ejection line for this model is displayed in Figure 3.21. The estimate for the amount of mass ejected is 44.7 kg (based on the ejection line).

Formulation Discussion

Table 3.2 summarizes the ejected mass, ejecta velocity, and crater depth for the validation experiment and its models. Immediately, one can see that the SPH formulation results are closer to the experiment for each of the quantitative parameters than those of the MMALE formulation. Indeed, this appears to match the qualitative description of the

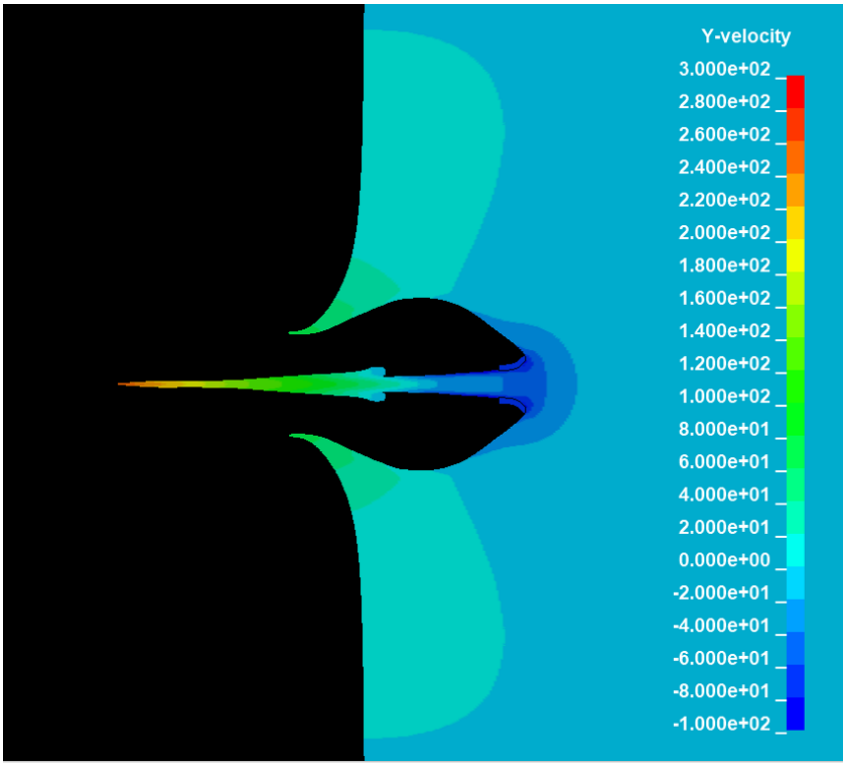

Figure 3.20: MMALE early-time plume velocity.

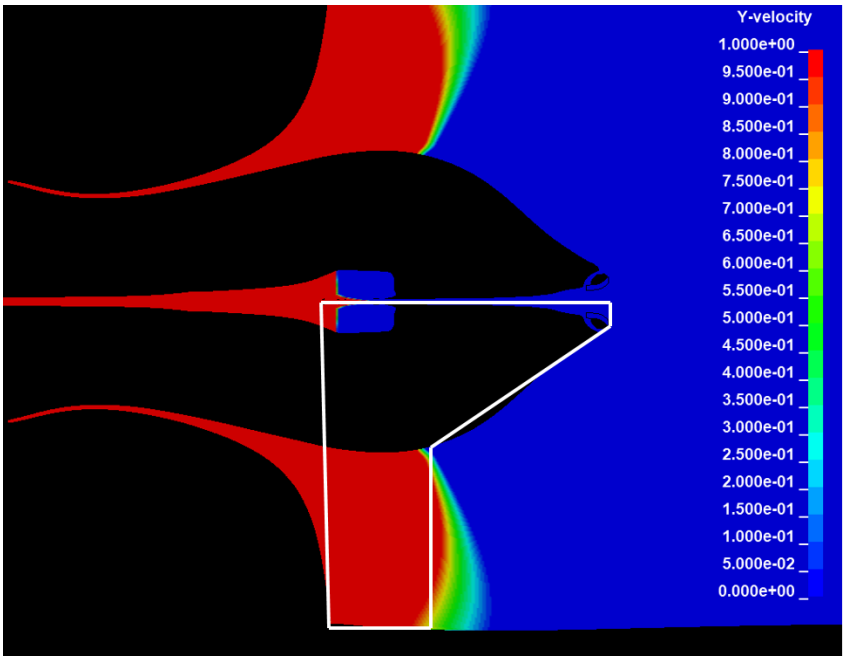

Figure 3.21: MMALE ejection line.

impact: the SPH results capture the surface eruption of the target and crater shape very well, even capturing (to some degree) the fracturing and spalling of ice across size scales. The MMALE model, with its purely Eulerian treatment, produces results on the same order of magnitude for each of the quantitative descriptors, but does not match well the shape or development of the crater. Since the crater does not match that of the experiment, one can conclude that the ejection processes also miss those of the experiment, therefore also the plume shape and velocity. The SPH model appears to better capture the behavior of ice through and after the ejection process, though the internal structure of the ejecta plume of the validation experiment is ultimately uncertain.

For the purposes of this study, the SPH model formulation is chosen to model impacts into ice and the associated ejecta plumes. The post-processing routine for particle splitting and scalar field creation, detailed in section 3.2.1, is therefore also adopted for the study of plume-probe interaction.

Table 3.2: Comparison Summary

Description	Experiment	SPH	MMALE
Ejected Mass	29.9 kg	28.3 kg	44.7 kg
Ejecta Velocity	545 $\frac{m}{s}$	400 $\frac{m}{s}$, est.	255 $\frac{m}{s}$
Crater Depth	5.7”	6.6”	12.2”

3.4 Full-Scale Impact Modeling

To recast the SPH model of the validation shot to a full-scale impact simulation (mimicking a viable mission into Europa) is straightforward, requiring only modifications to the penetrator mesh and size and number density of the ice target. A ‘nominal’ impact case is presented and analyzed. The penetrator (a solid model of which is portrayed in Figure 3.22) used for this model is 6 inches in diameter and has a mass of roughly 8 kg. It is set to impact at $1000\frac{m}{s}$ into a pseudo-infinite ice target. The ice target was sized to not influence or corrupt the cratering process by wave reflection. The majority of the cratering (or rather, most critical phases of cratering) takes place before a pressure

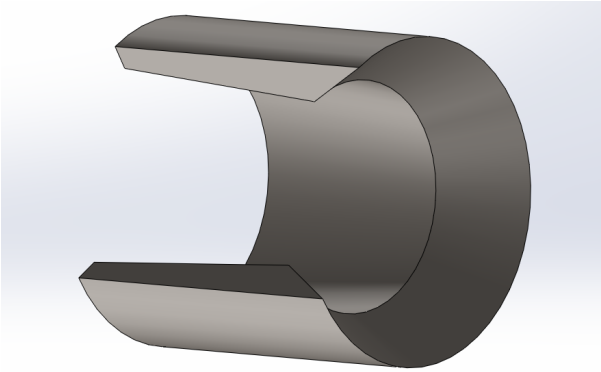

Figure 3.22: Cutaway of penetrator for full-scale nominal case.

Table 3.3: Nominal Full-scale Impact

Parameter	Value	Description
Penetrator L/D	1	Ratio of length to diameter
Nominal OD	6 in	Diameter of penetrator
Nominal ID	4.25 in	Diameter of internal surface
Knifde edge angle	30°	Relative to centerline
Penetrator material	AISI 4340	Steel alloy used for penetrator
Penetrator mass	8.01 kg	Penetrator mass only
Impact velocity	$1000\frac{m}{s}$	Estimated from high speed video
Target diameter	10 m	Diameter of ice target
Target depth	5 m	Depth of ice target

reflection wave can reach the areas of importance. As with the validation SPH model, the number density of the particles in this domain was chosen based on a 5%-criterion convergence study. A summary of the parameters used in this full-scale impact example is shown in Table 3.3.

Several stages of the impact are shown in Figures 3.23 to 3.25, with Figure 3.25 representing a 'fully developed' ejecta profile. Of note is that although the complete ejection has not happened at this latest state, the solver has flagged the large portions of the surface of the target as fragments (as marked by the regions bounded by the red cracks). The material in these regions is also labeled as ejecta. Also of note is the shape of the crater - it is shallow, gradual, and continuous, unlike that of the validation model, whose boundaries were greatly affected by the size of the domain and

its boundary conditions. The post-processing routine adopted for plume creation and extension receives and archives the state of the model at the 'fully developed' condition.

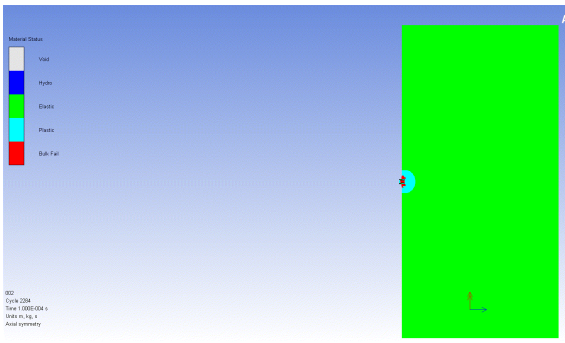

Figure 3.23: SPH Impact; $t = 1.0 \cdot 10^{-4}$ s.

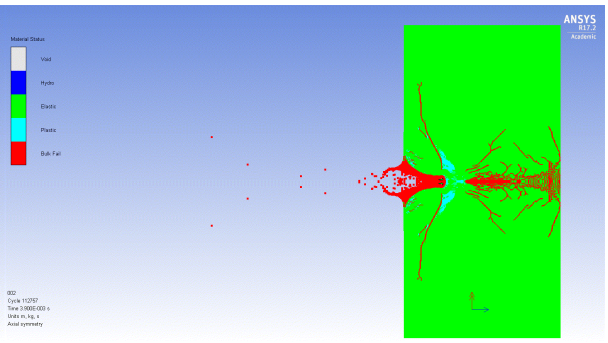

Figure 3.24: SPH Impact; $t = 3.9 \cdot 10^{-3}$ s.

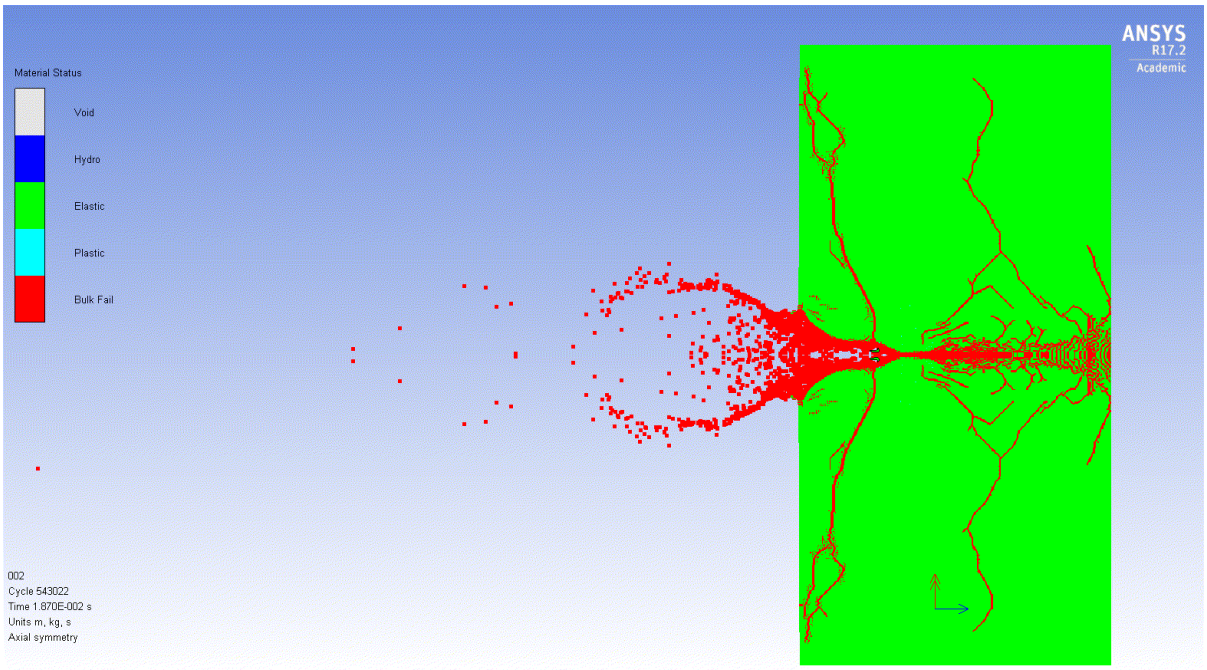

Figure 3.25: SPH Impact; $t = 1.87 \cdot 10^{-2}$ s.

Chapter 4

Payload-Ejecta Interaction

A method of obtaining a first-order-minimum approximation of the interaction of a probe equipped with ejecta brakes and an ejecta plume is desired for the purpose of quickly iterating on and optimizing a penetrator-probe kinetic deposition mission. The 'design space' for the initially uninformed includes staging distance (or time), ejecta brake size, probe mass (or payload mass fraction), payload impact speed, penetrator speed, impact angles, among several others. A method is desperately needed to give some insight into the trade-offs between some critical variables. These cannot be iterated upon easily, or at all. Penetrator geometry and material, for example, are known drivers to the formation and behavior of the ejecta, but a thorough study of the effects of different designs, materials, and the interactions of these parameters with the prior mentioned conditions would quickly consume all resources for this project and slow progress to a halt. Instead, a select few parameters will be analyzed and presented to give a glimpse of the capability of the modeling effort and possible directions forward.

4.1 Plume Extension and Characterization

For a particle tracking scheme, the ejecta is not immediately represented by a smoothed spatial field of properties (density, velocity, etc.). To fully capture the physical properties and behavior of the ejecta plume, the physical phenomena behind the shaping of the plume must be completed or fully developed. This means that the interactions between the penetrator and the medium would have no further influence on the ejecta, plume, or their other associated properties. To reach this state of 'fully developed', the time passed since impact will likely need to be significant, since material fails and is ejected well after the impact time stamp. For engineers, this is a difficult problem. The ejecta must be modeled at a high spatial resolution to capture local effects, but also at a wide range of times, often ending on the order of seconds or minutes after impact. An AUTODYN SPH impact simulation, with a domain spanning all involved physical space, for upwards of 1 second would take more than a few months of computational time with the resources allocated for this research. For this reason, approximations, concessions, and assumptions about the ejecta plume must be made to continue towards a solution of the engineering problem.

An important step is taken to gain independence from time-intensive (and limiting) hydrocode modeling. The SPH simulations are run until the mass flux across the impact plane of the simulation has decreased to the point where it becomes negligible (corresponding to a density roughly equivalent to the vacuum of space) or zero. This end time is typically on the order of 0.01 to 0.05 seconds for the presented full-scale simulations. Depending on the staging distance and relative speeds of the penetrator and probe, the dt between the penetrator and probe can range from sub-second to several seconds or even minutes. A program was constructed in MATLAB that imports the necessary data from the SPH input deck and output files to recreate and advect the ejecta plume (the methodology for which is given in section 3.2.1). This advection scheme is purely kinematic and does not follow a Navier-Stokes type of solution. The validity and application of the advection program is discussed in section 4.1.1.

4.1.1 Continuum Approximation and Analogous Atmosphere

To establish a means for the interaction of an ejecta plume and an assumed rigid body (spacecraft or probe with ejecta brakes), the method by which energy and momentum is transferred from the ejecta to the rigid body must be defined. The ejecta from the impact models is taken to be a continuous medium in this study. This assumption allows for smooth integration and eliminated the burden of tracking the associated momentum transfer from individual collisions. Further, the plume is assumed to be fully developed (non-accelerating) and does not self-interact. The plume can, however, still advect through space. Because of the treatment as a continuum, since the velocities at certain parts of the plume may differ, the shape of the plume can change and grow through time.

Because the ice is modeled as a continuous fluid, the change in shape and volume of the ice plume means that the advection of the ice through this scheme does not conserve energy (sum of thermodynamic and mechanical). However, satisfying the momentum and continuity conservation laws are sufficient to provide a first order estimate of the plume.

4.1.2 Plume Density Surfaces Databasing

For introduction to the mathematical continuum drag calculation model, the density is taken to be a multi-variate function that can be expressed as a density surface through time:

$$\rho = \rho\left(x, y, t\right) \tag{4.1}$$

The density surface at any point in time can is expressed as an interpolated and smoothed surface reconstructed from hydrocode outputs by the developed smoothing routine. A linear interpolant fit is chosen for drag calculations since they are efficient and well-behaved, though behavior near boundaries of data requires an interface tracking

algorithm to bound the advected mass. The state of the plume is saved to a 'database' to be called by the drag model. This effectively decouples the hydrocode model from the drag model.

4.2 1-D Mathematical Drag Model

A 1-D mathematical model is used to approximate drag on an arbitrary body as it interacts with a given ejecta plume. Because of the nature of the plume and the dynamics of the system, the model can be built as a ordinary differential equation with variable coefficients to be integrated by a standard Runge-Kutta integrator (such as ODE45 in MATLAB). The differential equation is standard in form, beginning from Newton's Second Law:

$$F = m \cdot a = m\frac{d^2y}{dt^2} \tag{4.2}$$

$$F = F_{gravity} + F_{drag} \tag{4.3}$$

The continuum approximation is used to write an expression for drag in terms of dynamic pressure:

$$F_{drag} = qc_DA = \frac{1}{2}\rho v^2 c_D A \tag{4.4}$$

In the framework of a transient probe and atmosphere in absolute space, this becomes:

$$F_{drag} = \frac{1}{2}\rho\left(x, y, t\right)\left(\frac{dy}{dt} - v_{plume}\left(x, y, t\right)\right)^2 \cdot c_D \cdot A \tag{4.5}$$

The coordinate y is the in the direction perpendicular to the impact plane or in the direction opposite of the impact. The density, ρ, is prescribed by the density surface at a give time t. The end equations should be a system of first order ODEs:

$$\frac{dy^2}{dt^2} = \frac{1}{m}\left(\frac{1}{2}\rho\left(x,y,t\right)\left(\frac{dy}{dt} - v_{plume}\left(x,y,t\right)\right)^2 c_D A - ma_{grav}\right) \tag{4.6}$$

This is further split into:

$$y_2(t) = \dot{y_1}$$
$$\dot{y_2} = \frac{1}{m}\left(\frac{1}{2}\rho\left(x,y,t\right)\left(y_2(t) - v_{plume}\left(x,y,t\right)\right)^2 c_D A\right) - a_{grav} \tag{4.7}$$

This form is easily implemented in a MATLAB script or a MATLAB Simulink visual program. The former is used for the ability to quickly run parametric studies with limited user input. Appendix B provides the drag calculation code used.

Syntactically, the model approximates the density at a given altitude as an average over the projected area of the probe's aerobraking surface. The velocity is extracted using a similar averaging scheme.

The 1-D model requires several inputs in addition to the independent and dependent variables. The inputs are interlinked and variable, hence the need for a numerical integrator. The complete set of inputs and their associated assumptions is discussed in sections 4.2.1 and 4.2.2. Figure 4.1 shows the high-level visual representation of the drag modeling tool with the associated inputs and solution to (4.7).

4.2.1 Model Parameters

Several parameters dictate the degree of loading, domains, and accuracy of the model. These parameters are chosen based on ease of implementation, efficiency, and applicability to the problem.

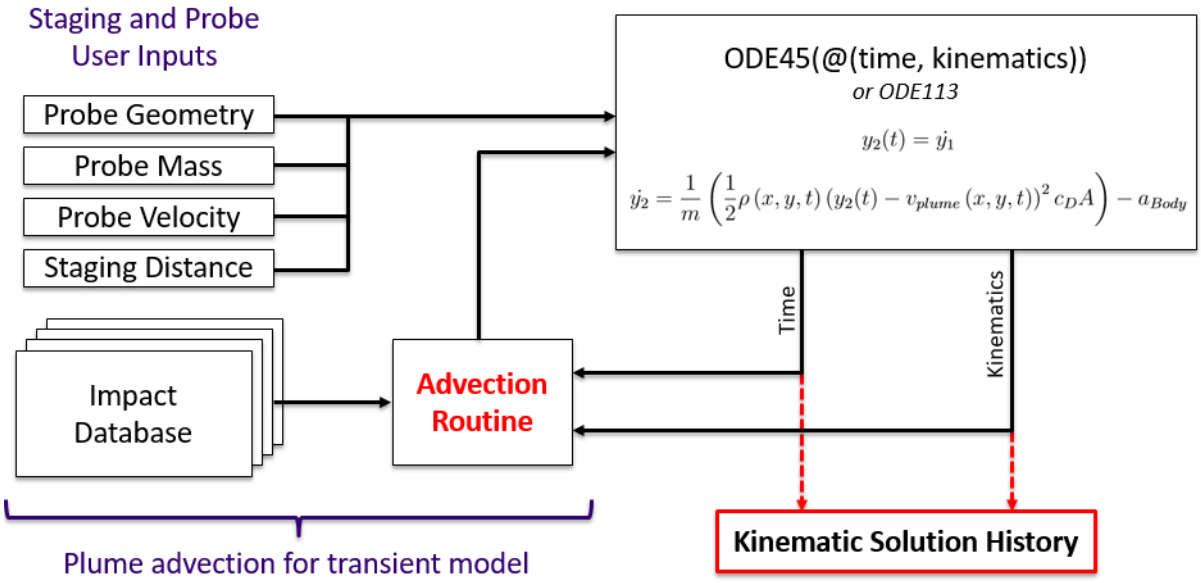

Figure 4.1: Visual representation of the drag modeling tool.

Probe Geometry

The model has a single degree of freedom: distance above the impact plane. The plume affects the motion of the probe through the projected area of the probe's braking system (conceptually rigid and cannot fail). The probe is completely defined by the radius (r) and total mass (m). The treatment of the radius is analogous to a radius in the cylindrical coordinate system.

Coefficient of Drag

The continuum-based approximation for drag is dependent on the dynamic pressure, projected area of the probe, and coefficient of drag. For subsonic continuum flow, the coefficient of drag for a flat plate perpendicular to the free-stream is approximately 2. This is the value used for the input c_D. This calls into question several aspects of the model: what defines 'sonic' in this flow regime? How does the flow interact with a probe? What is the Knudsen number of the flow, and how might that affect the calculation of drag? Because this model is a first-order approximation, these inconsistencies and

questions are noted, but not explored further at this time.

Acceleration Due to Gravity

Since a conceptual mission to Europa is presented, the value for the acceleration due to gravity is held constant at $-1.315\frac{m}{s^2}$, though this is over-exaggerated for large separation distances and far-field areas not close to the surface. The influence on the probe is negligible compared to that of the plume, but it is included for completeness.

Domain

A discretized physical domain is a required input to the model. The size of the domain is determined by the staging or separation distance of the penetrator or probe. This vector defines the y coordinate. In the x, or perpendicular, direction, the size is a fraction of the y direction, ranging from $\frac{1}{10}$ to $\frac{1}{2}$ depending on the degree of collimation of the plume. The grid itself is constructed using the meshgrid command in MATLAB.

Runge-Kutta Integrator

The depending on the solution characteristics, including time of solution, the differential equation is either ODE45, a 4th order Runge-Kutta integrator, or a low order ODE23 for stiff equations. The latter is useful for large variations in the solution magnitude, such as apparent discontinuities in density of the plume.

4.2.2 Model Initial Conditions and Probe-Penetrator Staging

The deceleration profile of the probe is heavily dependent on staging distance and initial conditions of the two stages. The model assumes that the stages have separated and that the penetrator has already impact the icy body.

Penetrator and Plume

A plume is chosen from the database of impact simulations of various penetrators. This decouples the model from the impact modeling and adds the flexibility of pairing any generated ejecta plume with any arbitrary 'mission' as prescribed by the model parameters and initial conditions. An additional benefit is the ability to change penetrator geometry or material without affecting downstream model programming. The workflow for including different plumes for coupled analysis (plume-probe) begins with running the full-scale impact models with the conditions required for the plume-probe interaction study. Several parsing scripts strip the outputs of the simulations and manipulate them to usable form in any plume-probe configuration. The 1-D drag model can call on any databased plume to include in the analysis.

Probe-Penetrator Separation Distance

Staging distance between the penetrator and the probe is critical to the interaction between the probe and plume. This is specified in the model as distance rather than a separation time. This separation distance is the location initial condition to the differential equation presented in (4.7). The separation distance is analogous to geometric altitude (referenced from the surface of the body of interest).

Probe Velocity

The second initial condition for (4.7) is the initial velocity of the probe as it enters the plume. This velocity is given in absolute space (relative to the surface of the body of interest, meaning the initial velocities of the penetrator and probe are negative. The impact velocity of the penetrator is set by the selection of one of the databased plumes.

4.3 Parametric Design Studies

A parametric study was conducted mapping out the interactions between staging distance, probe velocity, probe capture area, and probe mass for a 'nominal' penetrator impact. Compared are the trajectories of arbitrary probes as they interact with the plume and descend to the surface of the icy body. This parametric design study is presented not as a set of results for moving forward with mission design, but rather to exemplify the practicality and breadth of the parametric design and analysis tools created for this research.

A 'nominal' full-scale impact in the AUTODYN SPH framework will be used as the input to the parametric design and analysis tools. This nominal run, previously detailed in Section 3.4, is taken to be in a 'fully developed' state at 10 milliseconds after impact. At this time, the state of the particles are saved to memory through a databasing script. The format is standardized such that any arbitrary impact and plume can be loaded by the drag modeling tool for parametric design studies.

4.3.1 Drag Modeling Tool

The drag modeling tool takes vectorized inputs of the necessary initial and geometric conditions. The tool simply performs a full-factorial exploration of the inputs to the model, producing for the user a complete set of kinematics and peak loads for each of the modeled scenarios. In this example, kinematics for some of the scenarios are presented, as well as a rudimentary sensitivity study of peak deceleration through the plume as a function of staging distance between the penetrator and probe.

Table 4.1: Example Inputs to Parametric Design Study Tool

Input	Value	Description
Staging Distance	$[500, 1000, ...]$ m	Absolute altitude of drop, vectorized.
Probe Velocity	$-1000\frac{m}{s}$	Absolute velocity of probe
G	$-1.315\frac{m}{s^2}$	Acceleration due to gravity
$\frac{Mass}{Area}$	1	Ratio of mass to area (held constant)
r	$[1, 5, 10]$ m	Radius of probe capture area, vectorized.
$C_{d,brakes}$	2	Coefficient of drag for ejecta brakes

Table 4.1 displays the complete list of inputs for the drag modeling tool, less the databased input. Of note is that any input can be made into a vector, adding a dimension to the full-factorial design study.

The drag modeling tool advects the ejecta plume consistent with the kinematics of the probe as reported by the differential equation solver. This provides a hydrocode data-informed time accurate profile of what the behavior of an ideally staged mission may be.

4.3.2 Study on Effects of Staging Distance

Figures 4.2 and 4.3 show example bounding output kinematic traces from the drag modeling tool. Each of the plots are presented with each of the radii since the ratio of mass to area is constant ($\frac{M}{Area} = 1$) for these runs. This equates to an equivalent effective 'pressure' acting on the probes for each of the model runs. The traces, therefore, should overlap. Where they do not indicate local structure within the ejecta plume. See, for example, the difference between the 1 and 5 meter radius probe trajectories in Figure 4.2. The point of peak loading (analogous to 'max-Q') occurs at different times after separation. Likewise, the magnitude of peak loading is slightly less for the 1 meter radius probe, suggesting that the ejected material in the path swept by the probe is significantly different than that of the 5 meter or 10 meter radius probes. This trend is also reflected in the models run with larger staging distances, such as the set displayed in Figure 4.3.

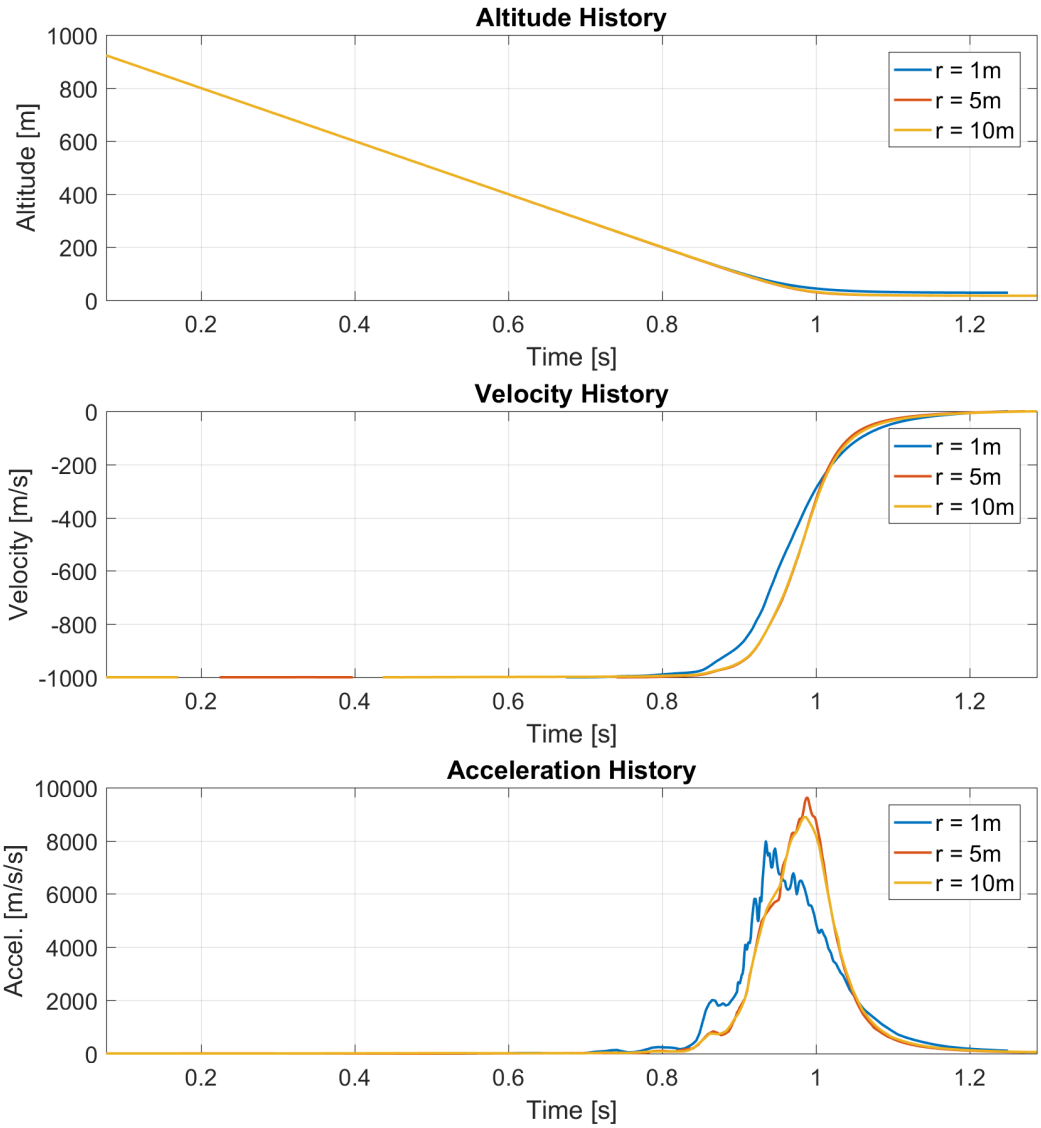

Figure 4.2: Kinematic traces of probe. Staging distance is 0.5km.

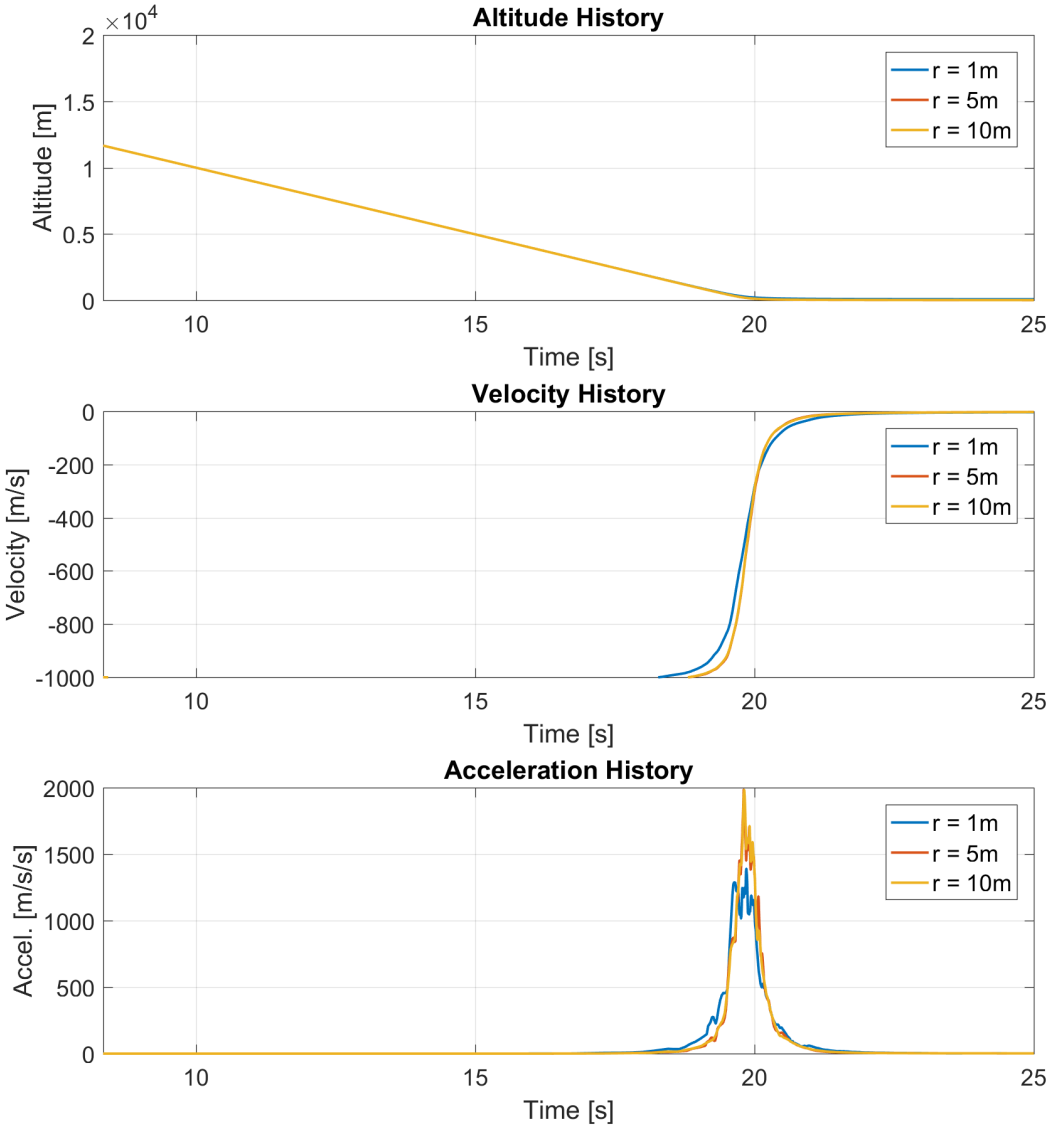

Figure 4.3: Kinematic traces of probe. Staging distance is 20km.

Very clearly one can see the dramatic staging-influenced effects on peak deceleration. Using the drag modeling tool, a more complete picture can be had by extending the vectorized input of staging distances and recording the probe responses. Figures 4.4 and 4.5 shows the behavior of the same three probe configurations across seven different staging distances. The behavior is expected - closer staging means a significantly higher plume density, and therefore more developed drag. On the opposite end of the spectrum, the large staging distances yield much less dense plumes, but the velocities of the plume and probe are such that the dynamic pressure developed is of the same order of magnitude.

Furthermore, it may be reasonable to expect peak deceleration will increase again with an increase of staging distance (note here the difference between peak deceleration and final velocity). As the ejecta plume becomes less and less dense, the probe has greater opportunity to reach the large, dense fragments expelled at low velocities about the point of impact. The drag modeling tool will model the interaction between these regions and the probe, but caution must be taken in interpreting these results since the governing physics may gravitate towards a collision-based regime (as opposed to the underlying continuum assumption used in this research).

4.3.3 Extensions of Drag Modeling Tool

Perhaps the greatest strength of the drag modeling tool is the ability to extend the inputs to the tool in a vectorized format, greatly increasing the scope of trade studies for both the physical mission design space and numerical settings, including fundamental assumptions. Examples of what may be studied through this tool are the effects of the coefficient of drag on the kinematics of the probe (fundamental to the assumptions made in this study), the inclusion of ablation of material from the probe (as a damage mitigation strategy), or the behavior of the models on different icy bodies (Ganymede versus Europa, etc.).

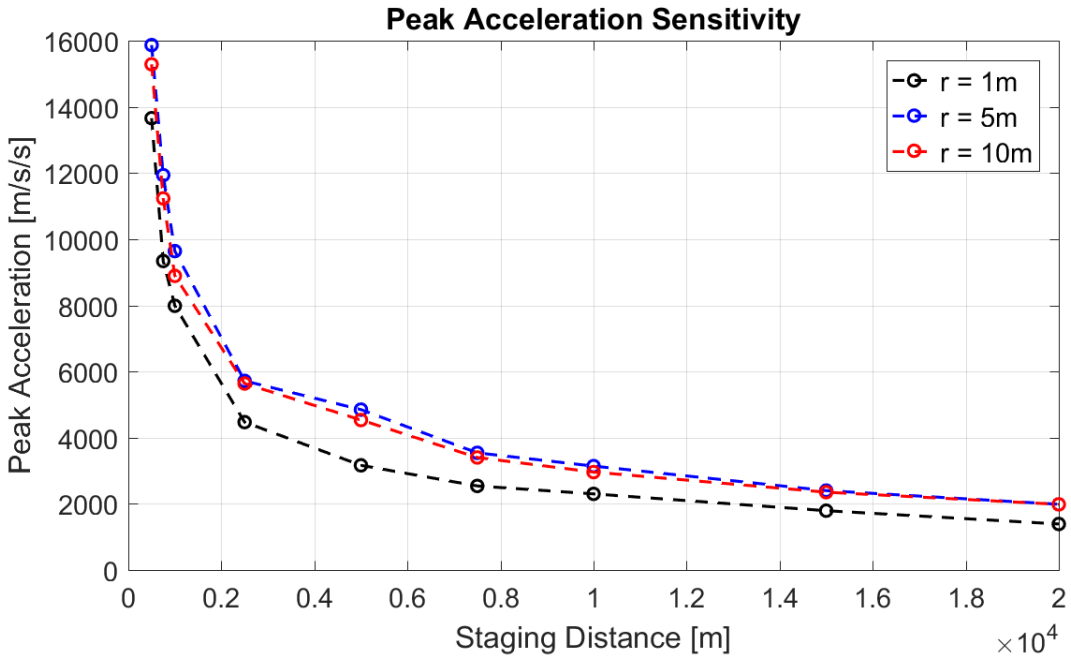

Figure 4.4: Peak deceleration through the ejecta plume as a function of staging distance.

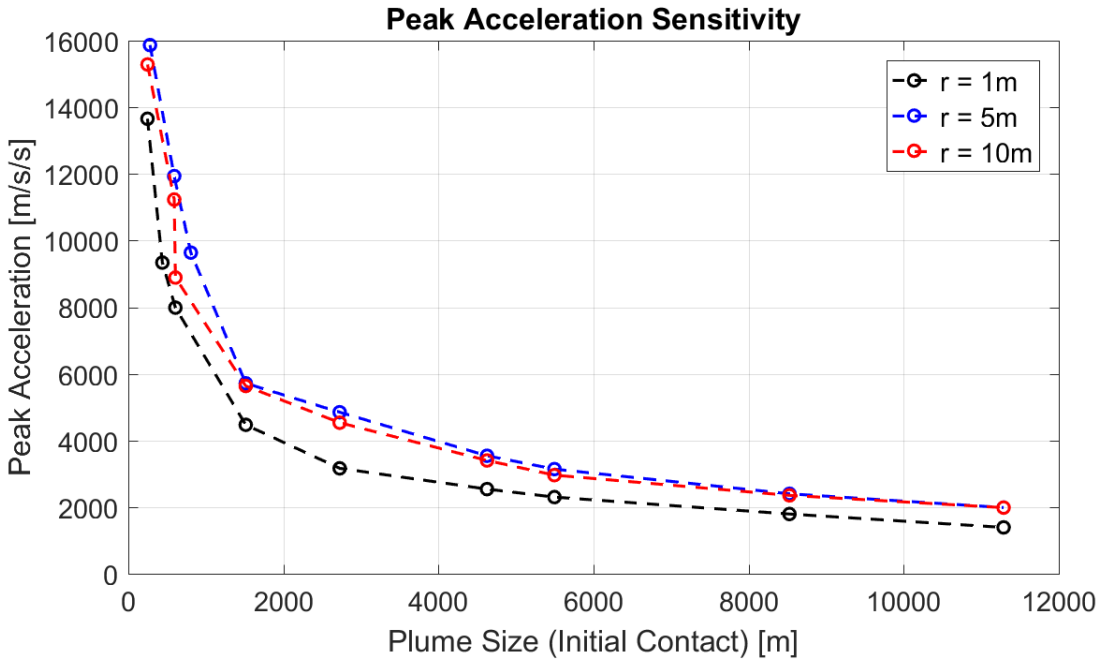

Figure 4.5: Peak deceleration through the ejecta plume as a function of plume size.

Chapter 5

Design of Future Experiments

Experimental work is needed to investigate the scaling associated with penetrators and payloads, specifically scaling of ejecta behavior with impact energy (velocity) and penetrator geometry. Experiments for both larger and smaller scales have been designed. A full-scale penetrator/payload low-speed drop into an ice sheet has been designed to investigate impacts into pseudo-infinite ice sheets and ejecta-payload interactions. A suite of small-scale light gas gun sub-bore projectile tests has also been laid out to investigate energy scaling.

5.1 Large-Scale Ice Field Experiments

A controlled and effective survey of boundary conditions in a laboratory setting is exceedingly difficult. Experiments in the University of Washington's Ram Accelerator Laboratory were performed to evaluate the effects of damping material along the boundary of the target cans with standard pink insulation foam and pykrete (an ice - sawdust mixture that behaves like a standard concrete). In an attempt to gain independence from boundary effects and give insight into the scalability of penetrator systems, a full-scale helicopter drop of staged articles has been planned.

Figure 5.1: Mock up of drop articles. From top to bottom: passively deployed hexcell ejecta brake article with steel-tipped penetrator, passively deployed Kevlar brake article with steel penetrator, timer-deployed Kevlar ejecta brake article with steel-tipped penetrator.

5.1.1 Article Overview and Operation

A set of two-stage penetrator-payload combination articles will be dropped (passive drop - the articles are not powered) from a helicopter at a reasonable altitude over an unconstrained ice field. The drop articles are designed such that at a certain point in its trajectory, the system will separate into penetrator and payload, with aerodynamic drag providing the separation and staging distance mechanisms.

The overall designs for these drop articles were driven by cost and reliability constraints. The first and smallest is pictured in Figure 5.1. The article is a variable density penetrator (steel tip and aluminum body) with a two inch diameter payload section. Cylindrical Hexcel crushable aluminum is used as an aerodynamic surface in free-flight and as an ejecta brake. The separation mechanism is passive and dependent on drop speed and altitude. By using slip-fit split rings to sabot the payload, a certain stagnation pressure will push the assembly out of the penetrator body and separate the stages. This is not a deterministic process or designed for a specific deployment altitude or speed. The second drop article was designed with the same operating principles in mind. This article is shown in Figure 5.1. Notable differences are the penetrator design and ejecta brake mechanism, which is common with the third (and only actively controlled) article.

The deployable ejecta brakes (articles 2 and 3) have four flaps or leaves that are free to extend out into the free stream. The position of the hinge for these flaps allows for the 'positive feedback' - the projected area of the flaps interacting with the free stream increases with deployment angle. Drag is proportional to projected area, further deploying the flaps. In this manner, the deployment of the flaps is passive provided that an initial 'kick' exists to expose the underside of the flaps to the free stream. This is achieved in the design and layout of the flaps in the stowed configuration. In the stowed configuration, the flaps are not truly shielded from the free stream flow conditions. The tips of the flaps are exposed, which, if the article has developed enough speed, provide enough exposed area to 'kick' the flaps further into the free-stream to complete the deployment and separation processes.

5.1.2 Ejecta Brake Mechanical Design

The ejecta brake assemblies are dynamic structural systems designed to decelerate a payload through transfer momentum from an ejecta plume. The mechanical design of the ejecta brake assembly went through several iterations to not only ensure that the mission performance requirements would be met, but also to minimize cost, promote manufacturability, and conform to the mission timeline.

The dynamic ejecta brake assemblies are made primarily of aluminum 7075 and 6061-T6 alloys to exploit their high strength to weight ratios. Each features prominently a central tubular shaft that acts as the guide surface for the brake deployment as well as the main load path for the drag force to act upon the rest of the probe. Each of the four ejecta brakes are made of slender, tapered rods, over which kevlar webbing is stretched and sewn on. The kevlar webbing acts as the contact surface between the ejecta and the probe.

Significant momentum is developed in the flaps deploying. In order to accommodate the potentially high angular velocity of the flaps as they near the end of the deployment

stroke, a linear compression spring makes contact with the flap deployment mechanism once they are roughly 35% deployed. The spring's solid (compressed length) corresponds to the flaps being perpendicular to the free stream flow.

5.1.3 Ejecta Brake Aeroelastic Response and Isolation

A requirement of a successful experiment includes the identification and isolation of aeroelastic effects on the drop article. The effects of Earth's atmosphere will dominate the response of the drop articles. Since no global atmosphere exists on icy bodies, these muddle any potentially observed cryobraking performance. The aeroelastic response for each of the articles, therefore, must be examined in full to distinguish between cryobraking and aerodynamic drag.

A program was developed within MATLAB's Simulink environment to model this interaction for an arbitrary penetrator-payload combination. The program is a standard integrator of the second order ordinary differential equation (freefall with drag) with variable coefficients. These coefficients are related to the projected area of the ejecta brake assembly, local density of the atmosphere, drop height, coefficient of drag, separation time (or distance), and mass properties of the articles. The code is 'actuated' through logic switches that activate deployment and staging to integrate the correct masses or drag for a given portion of the trajectory. Linkage kinematics (rigid body dynamics) also play an important role in the behavior of the system. Because of the design of the mechanism, the projected area of the ejecta brake flaps becomes a function of the geometry of the links and brakes, the stiffness of the shock spring, coefficient of drag, and dynamic pressure (the dependencies compound, too: dynamic pressure requires altitude and density information, etc.). The Matlab Simscape Toolbox is used in conjuction with Simulink to provide the linkage kinematics to the Simulink model in response to loads and vice versa. Representative geometry is used (to calculate inertias for links) with actual dimensions and hinge points. A representative model is developed and traced as a complete description of the program in section 5.1.3.

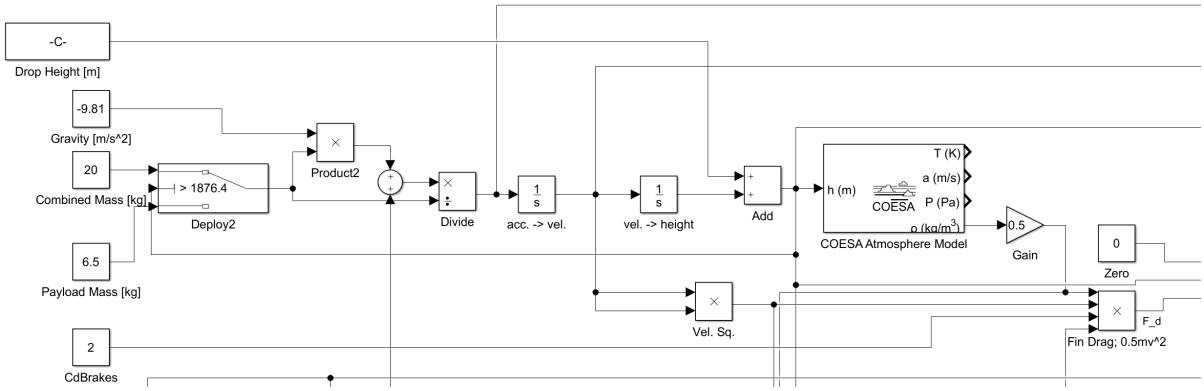

Figure 5.2: Representation of ODE with variable coefficients in Laplace domain.

Simulink Visual Code

Of note is that the geometry and aeroelastic response correspond to classical static aeroelastic divergence. While the general theory behind static aeroelasticity is relatively simple, the parameters required to complete (and be confident in) the analysis require extensive experimental tuning via wind tunnel testing. Quantities such as coefficient of lift of the aerodynamic surfaces, the lift curve slope, and mid aerodynamic chord would be prohibitively difficult to ascertain. As such, this method was considered second to the Simulink approach. The Simulink code, however, still requires deep knowledge of the system and its dynamics. The coefficient of drag used in the model is estimated, as are component masses, deployed brake area, and deployment time. The model, therefore, should be taken only as a first order estimate of the trajectory to distinguish between a success or failure of the cryobraking concept.

Figure 5.2 depicts the main section of the Simulink code (references to other sections can be seen exiting the bottom and right hand sides of the capture area - these are explained later). The integration of acceleration to height goes from left to right across the page. The major inputs are in a column on the left, beginning with the drop height in geometric altitude (absolute). Gravity is assumed constant at $-9.81\frac{m}{s^2}$. The combined penetrator-payload mass is next, followed by the payload-only mass, and finally the coefficient of drag of the ejecta brakes (drag from Earth's atmosphere in this case). Of

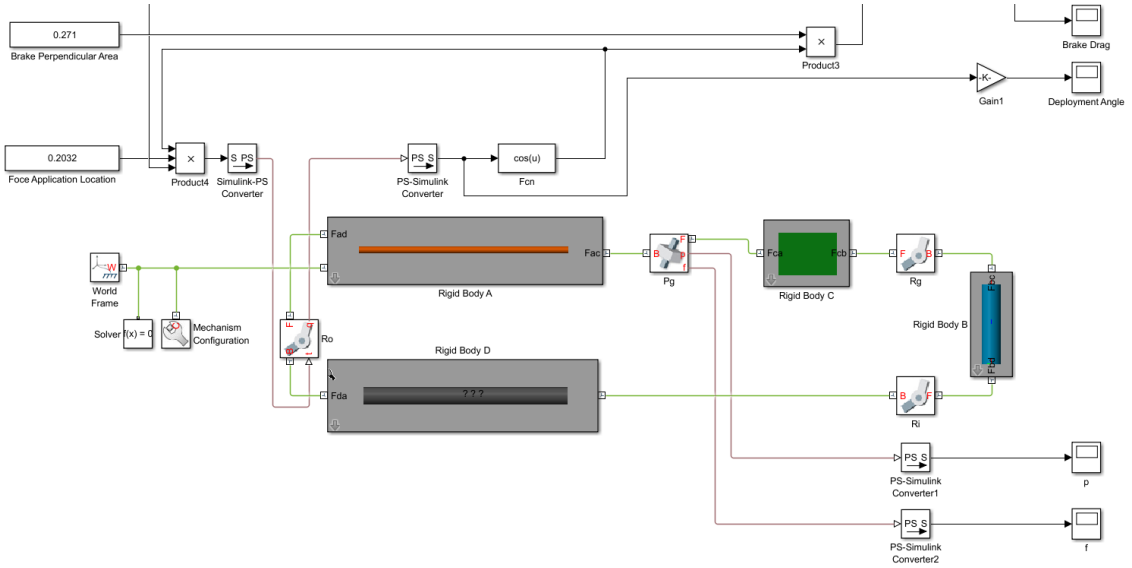

Figure 5.3: Representation of ejecta brake mechanism in SimScape with connection to the Simulink environment.

note is the deployment switch that selects the correct mass for the differential equation solver to use. At the beginning of the drop, the combined mass is used as the payload and penetrator are tethered together. Once deployed, controlled by the computer on-board and the switch in the Simulink code, the mass of the penetrator is jettisoned. Since the brakes will be deployed at this point, the force acting against the motion will resemble a step function of sorts. Simulink also possesses the option for a geometric atmospheric density lookup, used in this code as a lookup for the calculation of dynamic pressure in the drag force determination ($q_d = \frac{1}{2}\rho v^2$).

The Mathworks SimScape multibody dynamics solver is integrated into the Simulink code for approximation of the behavior of the ejecta brakes as they are deployed. This integration is shown in Figure 5.3. For the dynamics solver, the linkage is modeled as a crank-slider with range limited responses and sliding stiffness equal to that of the hardware spring, as shown in Figures 5.4 and 5.5. The direct comparison is shown in Figure 5.6. The links and sliding collar are equivalent masses to the actual hardware and are approximated (for inertias) as circular rods. Friction between the components is not taken (directly) into account, though there is damping added to eliminate chatter

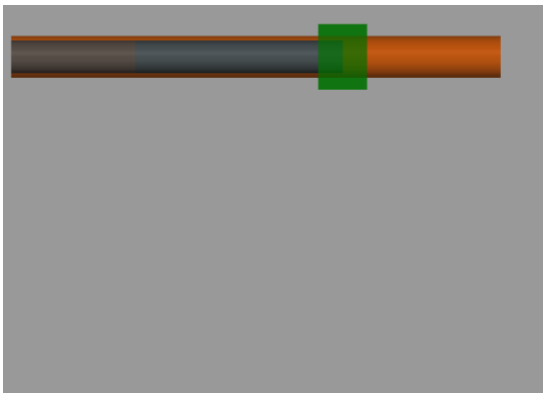

Figure 5.4: 'Stowed' configuration.

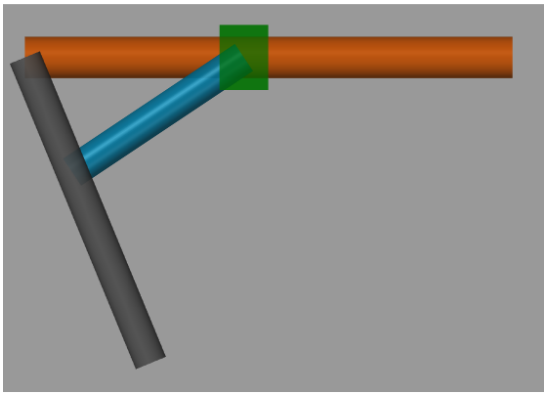

Figure 5.5: 'Deployed' configuration.

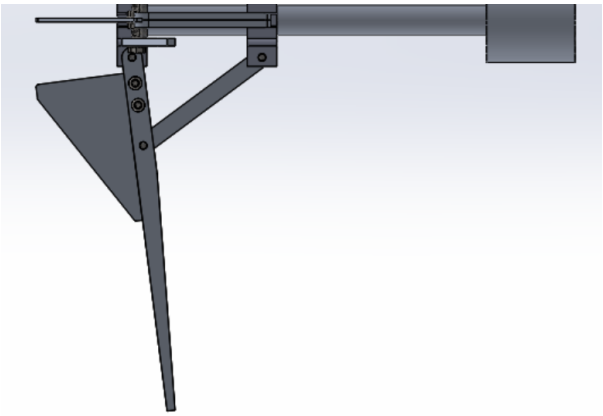

Figure 5.6: CAD image of deployed ejecta brake for comparison to SimScape model.

in the simulation. Only one link (of four) is modeled directly. Assumed is that the four links all open symmetrically without interference of off-axis loading. SimScape calculates are records the angular positions (and therefore velocities and accelerations) of the links. The displacements are used to calculate a projected area in the streamwise direction for drag calculation (performed by a simple cosine operation on the angular position signal).

A useful feature of Simulink is the ability to probe and plot any signal in the program with little effort. Since this is the case, the output data streams for probe kinematics (x, v, and a), body drag, brake drag, and brake deployment angle are all recorded and visualized simultaneously.

Simulink Code Example Output

To illustrate the use of the tool and its applications, an example is provided here. A complete set of inputs is shown in Table 5.1. The inputs are somewhat standard, though an exception is the specification of the altitudes of the drop, target, and deployment. During the actual event, these numbers will be very uncertain and that uncertainty will very likely propagate through to the performance of the staged articles. The kinematics of the payload-penetrator article described in Table 5.1 are shown in Figure 5.7 for the duration of the flight of the payload (the end of the trace marks 'impact').

There are a few phenomena embedded in the kinematic traces worth noting. First, because of the separation of the payload from the penetrator, a cusp exists in all traces. This occurs about 8 seconds after the drop for these conditions. Immediately after deployment initiates, the ejecta brakes swing open. The force retarding the motion of the payload increases dramatically and begins to slow the craft down. The velocity plot shows the deceleration of the craft to a new, significantly slower terminal velocity. Likewise, the altitude versus time plot clearly shows the less aggressive trajectory for impact.

These outputs not only shed light on the operation of the articles for deployment, but also provide valuable insight to article design should future articles be built for similar staged missions or trajectories. The MATLAB function **sim** (simulate) provides a way to interface with the Simulink visual code with the MATLAB traditional workbench. This is a very power tool since scripting in the workbench environment can allow for looping structures and rapid reconfiguration.

5.1.4 Experiment Obstacles

This experiment must overcome several obstacles to be successful. Most notable is the lack of flexibility for drop altitude or location. The articles have been designed for a certain altitude, meaning that any altitude drop that does not correspond to the design

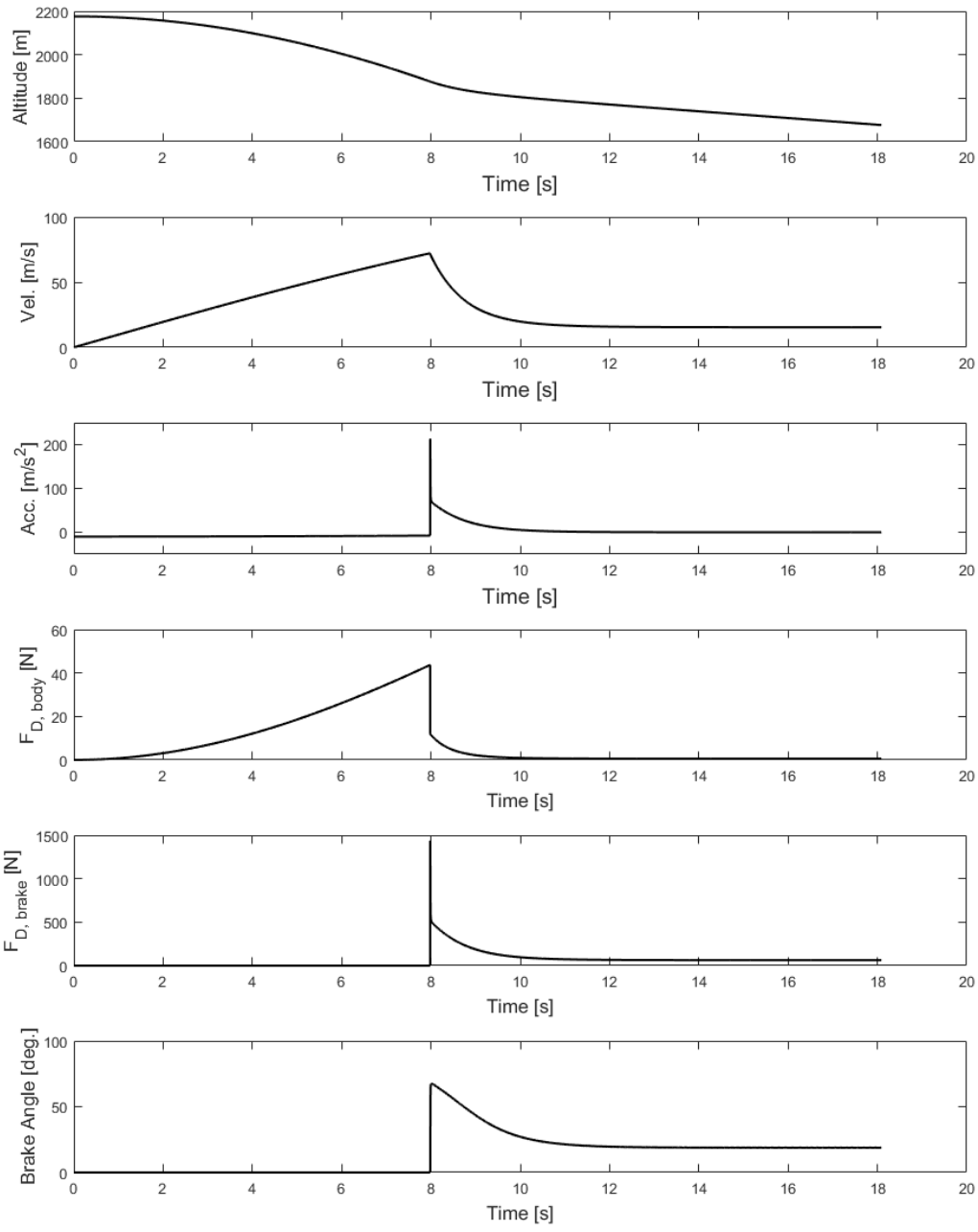

Figure 5.7: Payload kinematics during and after deployment.

Table 5.1: Example Inputs to Simulink Code

Input	Value	Description
Drop altitude	3700 m	Absolute altitude of drop
Deployment altitude	1876.4 m	Absolute altitude of deployment
Target altitude	1676.4 m	Absolute altitude of target
G	$-9.8066\frac{m}{s^2}$	Acceleration of gravity
M_{total}	20 kg	Combined penetrator and payload mass
$M_{payload}$	6.5 kg	Mass of payload only
$C_{d,brakes}$	2	Coefficient of drag for ejecta brakes
$C_{d,body}$	1	Coefficient of drag for payload body
A_{total}	$1.65 \cdot 10^{-2}$ m^2	Combined penetrator-probe cross-sectional area
$A_{payload}$	$4.65 \cdot 10^{-3}$ m^2	Probe cross-sectional area (stowed)
A_{brake}	2.71 m^2	Brake cross-sectional area (fully deployed)

altitude is an off-design case and has not been analyzed. The chance that the drop articles are released from a lower prescribed altitude is great, since the winds and visibility of drop zones may change at a moment's notice. If the drop height is low enough, the mechanism to deploy the ejecta brakes may not actuate (drag dependent, which would constitute a failure of the experiment. Therefore, while the structure of the ejecta brake assembly may be robust, the associated operability is very limited in scope and may prove to be critical to the mission.

Likewise, the deployment altitude of the eject brake assembly is very uncertain. The drop articles with this design can either be deployed passively (whenever enough drag has been established to 'kick' the brakes out) or actively, with a cable cutter/timer assembly. The former option has not been tested in a wind tunnel or with any dummy articles. The latter has been bench tested numerous times, but the uncertainty of the timer and cable cutter times propagates through to uncertainty in deployment altitude. Therefore, the experiment cannot have an altitude-dependent reporting of a metric as valid data.

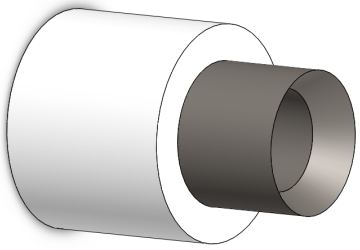

Figure 5.8: CAD rendering of sub-bore projectile (gray) and sabot (white).

5.2 Light Gas Gun Experiments

The continued use of the Ram Accelerator as a light gas gun will provide insights into scaling of hypervelocity impacts with impact energy, projectile geometry, and materials. The modeling efforts point towards material choice and deformation as significant, if not critical, contributors to the behavior of the ejecta plume. To keep the experiments in the same strain rate range of interest, the projectile material for LGG shots can be easily changed to a different aluminum alloy (since the densities will be similar). For example, aluminum 7075 has nearly double the yield strength in tension of aluminum 6061, but roughly equivalent density. This could potentially be extended to more dense materials, such as steels, with design modification to the projectile. For future experiments with dense materials, designs have been made for sub-bore projectiles. These physically smaller projectiles would have roughly the same mass as full-bore projectile, allowing for the same impact speed and strain rate in the ice. A CAD rendering of a sub-bore projectile is shown in Figure 5.8.

Steel is an interesting material choice because the hardness and strength of the steel can be altered dramatically with heat treatment. Effects of very hard projectiles are of interest especially in evaluating the behavior of the knife edge of the projectiles (how might the plume and penetration depth differ with hardness and strength of the projectile?). Naturally, the shape and angles of the entry and exit surfaces are also of interest. In examining the influences of these parameters on the cratering and plume creation, most critical is retaining the ability to isolate the response of single, discrete

changes in geometry. This is difficult because of the large number of experiments needed to adequately map out the design and response spaces of the projectiles - there is always the temptation to turn more than one knob at the time of the experiment. The most logical path forward is creating and adhering to a classical experiment design, whether that be a full or fractional factorial experimental program or a more complex Latin-Hypercube type experimental program.

Chapter 6

Discussion and Conclusion

6.1 Impact Modeling

Two impact model formulations representing the extremes of fluidic treatment were presented: the Smoothed Particle Hydrodynamic formulation, and the Multi-Material Arbitrary Lagrangian-Eulerian formulation. With one extreme, the fluidic treatment equated to a purely Lagrangian framework, complete with particle tracking. At the opposite extreme, the MMALE formulation is a purely Eulerian treatment of the fluidic response. Each formulation was used to model a validation impact experiment, where, in a controlled setting, a penetrator of known geometry and mass was propelled into an ice target at a known velocity. The Lagrangian perspective and treatment of the impact and ejecta modeled the validation experiment better than the Eulerian formulation. While this can be attributed to a number of different factors, the most relevant is undoubtedly the discretization and treatment of the ice medium through space. SPH models do not have grids, meshes, or anything of the sort, in effect relaxing the restrictions on the ice and allowing the ejection to occur as it may in natural processes. The Eulerian treatment, while consistent with the conservation equations and an equation of state, is confined to a computational grid. This grid introduces issues of necessary resolution,

boundary reconstruction, and stability that casts a shadow over the formulation for these applications.

The success of the SPH set of methods for impact modeling enabled progress to be made on modeling full-scale (or, rather, 'mission'-scale) impacts into icy bodies. An example full-scale SPH model was constructed and run for a significant amount of physical time to show the cratering and ejection processes in a pseudo-infinite domain (in contrast to a confined target, such as that of the validation experiment and models). Ejecta from this full-scale model was used as input to the 1-D drag model developed for this research.

The modeling deficiencies should be noted. Total energy of the system is only approximately conserved with thermodynamic effects neglected. This assumption may be valid if the kinetic energy is much greater than the thermal energy. The assumptions used in this study and their implications are noted and are suitable for engineering applications.

6.2 Drag Modeling

Drag modeling was accomplished through the solution of the drag differential equation. The solution of this equation was nuanced. A necessary prerequisite was knowledge of the 'transient atmosphere' through which the mission probe was passing. This atmosphere was constructed in two steps: first, the SPH particles were split in accordance with the conservation of mass and momentum. Second, the collection of particles were smoothed out onto a meshgrid data structure. The projection onto a computational grid allowed for an efficient interpolation of field variables, as needed by the differential equation solver. To ensure that the drag model was time accurate, the interaction between the plume and the probe was parameterized by time and was set as the independent variable for the differential equation solver. The resulting model is time accurate and incorporates the transients in the plume.

Since the impact model is decoupled from the drag model, the ability to quickly iterate

through scenarios and parameters was gained. The usefulness of this type of modeling was shown by a quick sensitivity study on the effects of staging distance (plume size) on peak deceleration of the probe.

This drag model relies heavily on the assumption that the plume is continuous. While this may be true in some regions of an ejecta plume, this is in general not the case. Study of the experimental impacts show clearly the different size scales of the ice particles as they are ejected from the target (note, however, that the high speed camera can not image the inside of the plume - only the external structure). With different particle sizes traveling at different velocities, the plumes have time and spatially-varying Knudsen numbers. A better treatment of the interaction between a plume and probe would take this into account, perhaps even recasting the Knudsen number as a field variable and the drag equation as a function of this parameter. The treatment of drag should tend towards tracking momentum transfer through particle collision in the rarefied and large-fragment regimes. The current treatment (with the continuum approximation used) do not take these considerations into account.

6.3 Parametric Analysis

Parametric design and analysis was made possible by virtue of the drag modeling and plume extension tools. The analysis efforts began with a study of the effects of staging distance (or plume height) on peak deceleration of an idealized probe as it passed through the plume. This analysis (from section 4.3) presented a set of cases where the aerial density of the probe was held constant ($\frac{Mass}{Area} = 1$) while the radius of the craft and staging distance was varied to map out this specific 2-D design space.

A clear trend is observed with the results from the parametric study - as staging distance (and plume height) increase, the magnitude of the peak deceleration decreases. The bounding cases presented ranged from roughly 16,000 m/s^2 to 2000 m/s^2, suggesting the possibility for tuning the loading seen on the probe by changing the penetrator and probe

staging. A goal of the research is to be able to invert the results of the numerical studies into design constraints. For example, a hypothetical design question may be asked: for a 25kg scientific payload that can survive a maximum of 500 Earth g's, how must one design the penetrator and probe to land on Europa? The presented parametric analysis curves for the nominal impact and plume point to a staging distance of about 5 km for a craft with an aerial density of 1 $\frac{kg}{m^2}$, which equates to probe brake capture radius of roughly 2.8 meters.

6.4 Tool Development

Several scripts and programs were created in MATLAB to assist in the automation of the research efforts presented here. Brief summaries of the most important tools are given in this section. The code for these tools is listed in Appendix B.

6.4.1 SPH Post Processing Tool

There exists a disconnect between ANSYS AUTODYN and the 1-D drag model. Several methods can be used to bridge this gap, but, in keeping with the theme of databasing and automation, a script was created to perform this task.

This tool evaluates the current state of the SPH model and extracts the kinematic and mass properties of each particle, assigning these variables to various fields in a particle object. With the necessary data imported into the MATLAB, manipulations on the particles is now possible (and is the basis for the drag model). The most important operation is to increase the number density of the particles as preparation for the advection and field creation functions. The particle splitting is dictated by simple conservation of mass and momentum checks. These checks are enforced per AUTODYN particle, ensuring that the sum of the split particles do not exceed the original particle's mass or momentum.

6.4.2 Advection and Field Creation Functions

Two of the most important elements of the drag model are embedded as functions: advecting the plume and creating the density field. Plume advection is based on free-molecular flow. Once the particles have been ejected from the target, assumed is that there are no interactions between particles, so the particles are stepped forward in time based on inherited kinematics from AUTODYN.

Immediately following advection of the particles, the function creating the density field is called. This function takes the list of partices and projects them onto a computational grid for smoothing. This projection and smoothing happens for every timestep of the drag model, and is therefore the bottleneck of the drag model program as a whole.

6.4.3 Drag Model

The 1-D drag modeling program performs arbitrary full-factorial numerical experiments. The full-factorial experiments are based on looping through several vectorized parameters (or dimensions). The program shell creates and initializes these loops based on the vectorized inputs and systematically calls the differential equation solver with the specified plume and probe conditions. The drag model shell calls the advection and field creation functions within the differential equation solver so that the program and calls are all self-contained and automatic.

6.5 Future Work

The presented research has created the framework necessary for preliminary mission design and analysis. Immediate future work includes creating more impact database entries to include in the numerical experiments with the drag model. Such impacts may vary impact speed, penetrator geometry, penetrator material, etc. These database entries

will serve as a larger array of 'initial conditions' for the drag modeling tool to sweep through (adding several more possible dimensions to the full-factorial study). These sets of simulations and models bring the program closer to being able to conduct a true optimization study on any parameter of interest. Likewise, the design space of this class of missions has never been mapped out - an incredible opportunity for this research to be applied on a significantly larger scale.

Of course, these models are only conceptual until results from the model can be validated. The experimental half to the research must continue to instill more confidence in the methods presented. Implied is both LGG laboratory experiments and full-scale terrestrial experiments to marry new data with new modeling capabilities.

Bibliography

[1] J. C. Niehoff and A. L. Friedlander, "Pioneer mars 1979 mission options," *Journal of Spacecraft and Rockets*, vol. 12, pp. 451–452, aug 1975.

[2] E. Schulson, "The structure and mechanical behavior of ice," *Journal of The Minerals, Metals, and Materials Society*, vol. 51, no. 2, pp. 21–27, 1999.

[3] W. Chen and T. Qiu, "Numerical simulations for large deformation of granular materials using smoothed particle hydrodynamics method," *International Journal of Geomechanics*, vol. 12, pp. 127–135, apr 2012.

[4] H. Kim and K. T. Kedward, "Modeling hail ice impacts and predicting impact damage initiation in composite structures," *AIAA Journal*, vol. 38, pp. 1278–1288, jul 2000.

[5] K. S. Carney, D. J. Benson, P. DuBois, and R. Lee, "A phenomenological high strain rate model with failure for ice," *International Journal of Solids and Structures*, vol. 43, pp. 7820–7839, dec 2006.

[6] R. Prakash, P. D. Burkhart, A. Chen, K. A. Comeaux, C. S. Guernsey, D. M. Kipp, L. V. Lorenzoni, G. F. Mendeck, R. W. Powell, T. P. Rivellini, A. M. S. Martin, S. W. Sell, A. D. Steltzner, and D. W. Way, "Mars science laboratory entry, descent, and landing system overview," in *2008 IEEE Aerospace Conference*, IEEE, mar 2008.

[7] A. O. Nier and M. B. McElroy, "Composition and structure of mars' upper atmosphere: Results from the neutral mass spectrometers on viking 1 and 2,"

Journal of Geophysical Research, vol. 82, pp. 4341–4349, sep 1977.

[8] A. Steltzner, D. Kipp, A. Chen, D. Burkhart, C. Guernsey, G. Mendeck, R. Mitcheltree, R. Powell, T. Rivellini, M. Martin, and D. Way, "Mars science laboratory entry, descent, and landing system," in *IEEE Aerospace Conference*, IEEE, 2006.

[9] e. a. K.P. Hand, "Europa lander study 2016 report," Tech. Rep. JPL D-97667, Jet Propulsion Laboratory, 2016.

[10] N. Longmate, *The Bombers: The RAF Offensive Against Germany, 1939-1945*. Hutchinson, 1983.

[11] R. H. Jr, "Defeating hard and deeply buried targets in 2035," Tech. Rep. AD1018630, Air War College Air University, Feb. 2012.

[12] C. Truitt, "Planetary penetrators for sample return missions," Master's thesis, University of Washington, 2016.

[13] T. Robinson, "Europa kinetic ice penetrator system for hyper velocity instrument deposition," Master's thesis, University of Washington, 2016.

[14] A. Serna, R. Dominguez-Tenreiro, and A. Saiz, "Conservation laws in smooth particle hydrodynamics: The DEVA code," *The Astrophysical Journal*, vol. 597, pp. 878–892, nov 2003.

[15] J. Donea and A. Huerta, "Arbitrary lagrangianeulerian methods," *Encyclopedia of Computational Mechanics*, pp. 413–437, Nov. 2004.

[16] L.-D. LSTC, "Keyword user's manual," *Version*, vol. 970, pp. 1–2, 2015.

Appendix A

Ice Material Models

Table A.1: AUTODYN Ice Material Model [4]

Input	Value
Density	$895 \frac{kg}{m^3}$
Elastic shear modulus	3.46 GPa
Yield strength	10.3 MPa
Hardening modulus	6.89 GPa
Bulk modulus	8.99 GPa
Plastic failure strain	0.35 %
Tensile failure pressure	-4 MPa

Table A.2: LS-DYNA Ice Tabulated Equation of State [5]

Volumetric strain [m/m]	Pressure [MPa]	Bulk modulus [MPa]
0	0	8963.2
$-7.693 \cdot 10^{-3}$	68.95	8963.2
$-3.125 \cdot 10^{-2}$	68.95	2206.3
-10	68.95	8963.2

Table A.3: LS-DYNA Ice Strain Rate Sensitivity [5]

Strain rate $[s^{-1}]$	Stress scaling
1.0	1.0
10.0	1.25660
100.0	1.51320
200.0	1.59044
300.0	1.63562
400.0	1.66768
500.0	1.69255
600.0	1.71287
700.0	1.73005
800.0	1.74493
900.0	1.75805
1000.0	1.76979
1100.0	1.78042
1500.0	1.81498
10000.0	2.02639

Table A.4: LS-DYNA Ice Strength Properties [5]

Input	Value
Density	$895\frac{kg}{m^3}$
Young's modulus	9.31 GPa
Initial compressive flow stress	172.4 MPa
Initial tensile flow stress	17.24 MPa
Plastic tangent modulus	6.89 MPa
Poisson's ratio	0.33
Pressure cut-off, compression	4.93 MPa
Pressure cut-off, tension	0.433 MPa

Appendix B

Drag Model

B.1 Hydrocode Interface and SPH Post-Processing

SPH Particle Extraction

```
function [ SPH,ts ] = get_particles( filename,s_trigger,p_trigger )

% Goals are to strip the SPH part of the necessary kinematics to recreate
% an effective atmosphere. We are only interested in things that have, or
% are in the process of, being ejected - 'free molecular flow'

% First we open the desired .prt file nad begin parsing:
fid = fopen(filename);
line_number = 0;
start_line = 0;
end_line = 0;
loop = 0;
time = 0;

ts = []; % the timestamps are empty

% we need to get the cycle numbers and time stamps for the .prt file. needs
% to be arbitrary. Since we're concerned with SPH particles only, we can
% exploit the format of the file to grab the necessary indices and build
% the matrices

% First pass-though for finding the size of the matrix and the structure of
% the .prt file.
while ~feof(fid)
    dataline = fgetl(fid);
```

```
    line_number = line_number + 1;

    % skip empty lines:
    if isempty(dataline)
        continue;
    end

    % quick comparison to start trigger:
    if dataline(1) ~= s_trigger
        continue;
    end

    % at this point we should have a line with the cycle and timestamp.
    % Need to make sure it is from the correct part or subgrid
    if dataline(84:84+length(p_trigger)-1) ~= p_trigger
        continue;
    end

    %Process this block and continue on.
    loop = loop + 1;
    if loop == 1 % if this is your first time here:
        time = time + 1;
        ts(time) = str2num(dataline(21:31)); % populate the first timestamp
        SPH_count = str2num(dataline(127:end));
    end

    if str2num(dataline(21:31)) == ts(time)
        continue;
    else
        time = time + 1;
        ts(time) = str2num(dataline(21:31));
    end

    start_line = loop;

end
fclose(fid);

%% we have the particle count and the timestamps for the history.
% now we need to create the matrices for the particles and populate them
% with the correct data.

% Structure: SPH(time, number, {x-loc, y-loc, x-vel, y-vel, density})
SPH = zeros(length(ts),SPH_count,5);
% we need to reopen the file and search for the cycle trigger and match
% timsteps

fid = fopen(filename);
p = 0;
while ~feof(fid)
    dataline = fgetl(fid);
```

```
    % skip empty lines:
    if isempty(dataline)
        continue;
    end
    % quick comparison to start trigger:
    if dataline(1) ~= s_trigger
        continue;
    end
    % Need to make sure it is from the correct part or subgrid
    if dataline(84:84+length(p_trigger)-1) ~= p_trigger
        continue;
    end
    % at this point the data will be piecewise continuous until the next
    % part, timestep, or end of file.

    % get the local time:
    local_time = str2num(dataline(21:31));
    I = find(ts == local_time); % get the index for this time stamp

    % since we have found the header and are done with it, we can move onto
    % stripping the data:

    % skip the first 6(+1 real) lines:
    for j=1:7
        dataline = fgetl(fid);
    end

    while ~isempty(dataline) && ~feof(fid)
        particle = str2double(dataline(1:6)); % particle, or J, number
        SPH(I,particle,1) = -str2double(dataline(20:31)); % x-location
        SPH(I,particle,2) = str2double(dataline(32:43)); % y-location
        SPH(I,particle,3) = -str2double(dataline(44:55)); % x-velocity
        SPH(I,particle,4) = str2double(dataline(56:67)); % y-velocity
        SPH(I,particle,5) = str2double(dataline(68:end)); % density
        dataline = fgetl(fid);
    end

    disp(['Getting Particles: ' num2str(particle/SPH_count*100) '%'])

end
fclose(fid);
disp('Finished SPH extraction.')

end
```

SPH Ejecta Extraction

```
function [ ejected ] = getEjecta( SPH,thresh )
% criteria for ejection is having appreciable negative x-velocity
% just look for them:

ejected = zeros(length(SPH(1,:,1)),length(SPH(1,1,:)));
num_ejected = 0;
for j=1:length(SPH(1,:,1))
    if SPH(1,j,3) > thresh && SPH(1,j,4) > 0
        num_ejected = num_ejected + 1;
        ejected(num_ejected,:) = SPH(1,j,:);
    end
end

ejected = ejected(1:num_ejected,:);

end
```

SPH Particle Splitting

```
function [ split ] = getSplitParticles( ejected,sf,radius,override )
% splits the SPH particles into many particles. Conserves mass, momentum.

% loop through the points listed in 'ejected'. Assign initial mass
% ('unity'), calculate momentum, calculate kinetic energy.

% sf = split factor

% radius = radius of influence for SPH particles that have not yet been
% split

split = zeros(length(ejected(:,1))*sf,length(ejected(1,:)));

if override
    split = ejected;
    return
end

for j=1:length(ejected(:,1))
    local_mom = sqrt(ejected(j,3)^2 + ejected(j,4)^2)*ejected(j,5);
    p_mom = local_mom/sf;

    local_split = zeros(sf,5);
    % for each SPH particle, split it into sf number of points. for each of
    % these, determine the x,y,u_x,u_y. The mass of the particle will be
    % backed out from the split particle's momentum. Only worry about
    % x-momentum (direction of impact)

    for k=1:length(local_split(:,1))
        % Columns of local_split:
        % 1 - x-location
        % 2 - y-location
        % 3 - x-velocity
        % 4 - y-velocity
        % 5 - density

        dx = cos(2*pi*rand(1,1))*radius;
        dy = sin(2*pi*rand(1,1))*radius;

        local_split(k,1) = ejected(j,1) + dx;
        local_split(k,2) = ejected(j,2) + dy;
        while local_split(k,2) < 0
            % ensure new location is valid (2d axisymmetric domain)
            dy = sin(2*pi*rand(1,1))*radius;
            local_split(k,2) = ejected(j,2) + dy;
        end
        D = sqrt(dx^2 + dy^2);

        local_split(k,3) = D/radius*rand(1,1)*ejected(j,3);
```

```
        local_split(k,4) = D/radius*rand(1,1)*ejected(j,4);
        local_split(k,5) = p_mom/sqrt(local_split(k,3)^2 + ...
            local_split(k,4)^2);
    end

    split(sf*(j-1)+1:sf*j,:) = local_split;

end

end
```

B.2 Advection and Drag

1-D Drag Model Shell

```
%% script to post-process the AUTODYN .prt file for SPH particles
% Goals are to strip the SPH part of the necessary kinematics to recreate
% an effective atmosphere. We are only interested in things that have, or
% are in the process of, being ejected - 'free molecular flow'

clear all, close all, clc;

% First we open the desired .prt file nad begin parsing:
filename = 'example.prt'
s_trigger = 'C'; % start trigger
p_trigger = 'Target'; % part trigger

SPH = get_particles(filename,s_trigger,p_trigger);
override = 0;
%%
figure(1)
plot(SPH(1,:,1),SPH(1,:,2),'ko')
title('AUTODYN Extracted Particles')

thresh = 5; % m/s
ejected = getEjecta(SPH,thresh);
figure(2)
plot(ejected(:,1),ejected(:,2),'ko')
title('Ejected Particles')

%% Split the particles
split_factor = 5; % number of sub-particles per particle
radius = 1; % radius of influence for SPH unsplit particles, meters
ejected = getSplitParticles(ejected,split_factor,radius,override);
figure(3)
plot(ejected(:,1),ejected(:,2),'ko')
title('After particle splitting')

%% Advect, get field, get drag:

% specify initial conditions:
init_v = -1000; % m
%h_tab = [1000 2500 5000 7500 10000];
%h_tab = [500 750];
h_tab = [25000 30000];
p_size = 0.015;

% specify the craft properties:
m_ratio = 1;
rtab = [1 5 10]; % m
mtab = (pi.*rtab.*rtab).*m_ratio;
c_d = 2.0;
```

```
g = -1.315; % m/s^2

% initialize structure counter
count = 27;

for p=1:length(h_tab)
    height = h_tab(p);
for q=1:length(mtab)

    % set structure count
    count = count + 1;

    % set geometry, masses:
    r = rtab(q);
    m = mtab(q);
    a = pi*r^2;

    % Quickly find the initial time
    v_plume = max(abs(ejected(:,3)));
    start_t = (-height/(init_v - v_plume)) - 0.25;
    end_t = height/abs(init_v) + 5; % s

    % set the initial conditions:
    tspan = [start_t end_t];
    y0 = [height + start_t*init_v init_v];

    % call the ODE solver:
    options = odeset('RelTol',1e-4,'AbsTol',1e-6,'Events',@eventing);
    [t,y] = ode45(@(t,y) ...
        getDrag(t,y,g,r,a,m,c_d,ejected,p_size), tspan, y0, options);

    history(count).time = t;
    history(count).disp = y(:,1);
    history(count).vel = y(:,2)
    history(count).accel = gradient(y(:,2), t(:));

    figure(5),
    subplot(3,1,1), hold on;
    plot(history(count).time,history(count).disp)
    title(['Position of M/Area = ' num2str(m_ratio) ' craft.'])
    drawnow;

    subplot(3,1,2), hold on;
    plot(history(count).time,history(count).vel)
    title('Velocity')
    drawnow;

    subplot(3,1,3), hold on;
    plot(history(count).time,history(count).accel)
    title('Acceleration')
    drawnow;
```

```
    % permanent storage:
    outfile = strcat(num2str(count),'.dat');
    data = [history(count).time history(count).disp ...
            history(count).vel history(count).accel];
    conditions = [h_tab(p) mtab(q) init_v m_ratio];
    csvwrite(outfile,[conditions; data]);
end
%% Visualization
figure(5)
subplot(3,1,1), hold on;
plot([0 end_t],[0 0],'k-')
xlabel('Time, s');
ylabel('Distance above impact plane, m')
legend('r=1.0m','r=5m','r=10m')

subplot(3,1,2)
ylim([y0(2) 0]);
xlabel('Time, s');
ylabel('Speed, m/s')
legend('r=1.0m','r=5m','r=10m')

subplot(3,1,3)
xlabel('Time, s');
ylabel('Acceleration Magnitude, m^2/s')
legend('r=1.0m','r=5m','r=10m')

outfile = strcat(num2str(p),'.png');
saveas(gcf,outfile);
end
```

ODE Anonymous Drag Function

```
function [ dydt ] = getDrag( t,y,g,r,a,m,c_d,ejected,p_size )
    % Use the staging distance to compute new meshgrid:
    lx = y(1); % meters
    ly = max([y(1)/3 r]); % meters
    [field,vel,X,Y] = getField(t,lx,ly,ejected,p_size);

    % radial profile:
    profile = linspace(0,r,ceil(r*2));
    dr = profile(end) - profile(end-1);
    A_band = zeros(size(profile));
    A_band(1) = pi*dr^2;
    for j=2:length(A_band)
        A_band(j) = pi*((profile(j)+0.5*dr)^2 - (profile(j)-0.5*dr)^2);
    end

    % average density:
    rho_A = zeros(size(profile));
    for j=1:length(profile)
        local_rho = interp2(X,Y,field',y(1),profile(j));
        rho_A(j) = local_rho*A_band(j);
    end
    rho = sum(rho_A)/(pi*r^2);

    % average velocity, momentum based:
    local_mom = 0;
    for j=1:length(profile)
        local_vel = interp2(X,Y,vel',y(1),profile(j));
        local_mom = local_mom + local_vel*rho_A(j);
    end
    if rho == 0 || isnan(rho)
        vel = 0;
        rho = 0;
    else
        vel = local_mom/(rho*pi*r^2);
    end

    % set up the differential equation:
    F_d = (1/2)*rho*(vel - y(2))^2*a*c_d;
    dydt = zeros(2,1);
    dydt(1) = y(2);
    dydt(2) = F_d/m + g;
    disp(['Time: ' num2str(round(t,3)) ' Position: ' ...
        num2str(round(y(1),3)) ' V_craft: ' ...
        num2str(round(dydt(1),3)) ' Rho: ' ...
        num2str(round(rho,3)) ' V_plume: '...
        num2str(round(vel,3)) ' F_d: ' ...
        num2str(round(F_d,3)) ' accel: ' ...
        num2str(round(dydt(2),3))])
end
```

Advection Routine

```
function [ field,vel,X,Y ] = getField( t,lx,ly,ejected,p_size )

%% Advect and see what it looks like
ejected(:,1) = ejected(:,1) + ejected(:,3).*t;
ejected(:,2) = ejected(:,2) + ejected(:,4).*t;

%% Create a meshgrid, smooth over smoothing length scale,

% go around a meshgrid and find distances to cell center location

[X,Y] = meshgrid((0:lx/600:lx),(0:ly/200:ly));
field = zeros(size(X(:,:)'));
vel = field;

for j=1:length(X(1,:))
  %   percent = j/length(X(1,:))*100
    for k=1:length(Y(:,1))
        N = 0;
        local_mass = 0;
        local_mom = 0;

        % Location of point
        x1 = X(k,j);
        y1 = Y(k,j);
        sr = max([x1/(10) 10]); % smoothing radius, meters

        for l=1:length(ejected(:,1))

            % Location of particles
           x2 = ejected(l,1);
           y2 = ejected(l,2);

           distance = sqrt((y2-y1)^2 + (x2-x1)^2);

           if (distance < sr)
               N = N+1;
               local_mass = ejected(l,5)*p_size^2*pi/4 + local_mass;
               local_mom = sqrt((ejected(l,3))^2+(ejected(l,4))^2)...
                   *ejected(l,5)*p_size^2*pi/4 + local_mom;
           end
        end

        if N <= 0.1
            field(j,k) = 0;
            vel(j,k) = 0;
        else
            field(j,k) = local_mass/(pi*sr^2);
            vel(j,k) = local_mom/local_mass;
        end
```

```
    end
end


log_field = log10(field+1e-12);

figure(100)
pcolor(X,Y,log_field'), shading interp, colorbar;
title(['Ejecta Plume at ' num2str(t) ' seconds']);
drawnow;

end
```